Mineralogical, Fluid Inclusion and Multiple Isotope (H-O-S-Pb) Constraints on the Genesis of the Sandaowanzi Epithermal Au-Ag-Te Deposit, NE China

Degao Zhai[1, 2*], Jiajun Liu[1], Anthony E. Williams-Jones[2], Stylianos F. Tombros[3], Nigel J. Cook[4]

[1]*State Key Laboratory of Geological Processes and Mineral Resources & School of Earth Sciences and Resources, China University of Geosciences, Beijing, 100083, China*

[2]*Department of Earth and Planetary Sciences, McGill University, 3450, Quebec, Canada*

[3]*Department of Geology, University of Patras, Rion, Patras, 26500, Hellas*

[4]*School of Chemical Engineering, University of Adelaide, Adelaide, S.A. 5005, Australia*

[*]Corresponding author: dgzhai@cugb.edu.cn

Submitted to: *Mineralium Deposita*

10th, Jan, 2018

Zhai, D. G., A. E. Williams-Jones, J. J. Liu, S. F. Tombros, and N. J. Cook.
"Mineralogical, Fluid Inclusion, and Multiple Isotope (H-O-S-Pb) Constraints on the Genesis of the Sandaowanzi Epithermal Au-Ag-Te Deposit, Ne China."
Economic Geology 113, no. 6 (Sep 2018): 1359-82. http://dx.doi.org/10.5382/econgeo.2018.4595.

Abstract

The Sandaowanzi gold deposit in the Great Hinggan Range Metallogenic Belt, NE China, is unusual for the fact that the mineralization takes the form of Au- and Ag-bearing tellurides. This mineralization, which constitutes a resource of 28 t Au, is hosted in 20 NW-trending, syntaxial, layered quartz veins and tension gashes within almost synchronous trachyandesites and andesitic breccias that overlie the Sandaowanzi monzogranite. Alteration halos are developed around the quartz veins and tension gashes. They consist of an inner silicic zone, two intermediate zones containing quartz-illite and quartz-adularia, and an outer zone containing a quartz-calcite-kaolinite-chlorite assemblage.

Fluid inclusion microthermometric data reveal that the Sandaowanzi ores precipitated from moderate-temperature (210º to 280°C), low pressure (70 to 130 bars) and low to moderate salinity (mostly <6.0 wt.% NaCl equiv.) hydrothermal fluids. Temperature and pressure are interpreted to have decreased with the evolution of the system. The $\delta^{34}S_{H2S}$ (-2.2 to -0.2‰) values indicate that the sulfur is of magmatic origin and suggest that it was leached by the ore fluid from the host volcanic rocks. A magmatic origin is also interpreted for the metals, based on Pb isotope data (i.e., a $^{206}Pb/^{204}Pb$ value of 18.2366 to 18.3146, a $^{207}Pb/^{204}Pb$ value of 15.5404 to 15.5624 and a $^{208}Pb/^{204}Pb$ value of 38.0901 to 38.2293). In contrast, the $\delta^{18}O_{H2O}$ (-13.6 to -7.6‰) and δD_{H2O} (-127 to -96‰) values indicate that the hydrothermal fluids are dominantly meteoric. Physicochemical modeling shows that sulfidation of the host rocks (decrease of $\alpha_{HS^-(aq)}$) and condensation of the H_2Te vapor (increase of $\alpha_{HTe^-(aq)}$) were the dominant controls on the precipitation of the Au- and Ag-telluride ores. The generation of a H_2Te vapor is mostly derived from a magma degassing, and the close genetic relationship between the gold-telluride ore formation and the coeval alkaline magmatism is helpful to understand gold-telluride ore genesis in comparable conditions.

Key words: Gold-telluride deposit; Fluid inclusion; Isotope geochemistry; Sandaowanzi; NE China

Introduction

In most epithermal gold deposits, telluride minerals are minor or absent; only a few deposits are dominated by telluride minerals, e.g., Cripple Creek (Kelley et al. 1998), Emperor (Pals and Spry 2003), Golden Sunlight (Spry et al. 1997), Acupan (Cooke and McPhail 2001), Săcărîmb (Ciobanu et al. 2008), Panormos Bay (Tombros et al. 2010), Kochbulak (Kovalenker et al. 1997), Porgera (Richards and Kerrich 1993) and Gies (Zhang and Spry 1994). Telluride-dominant epithermal

Zhai, D. G., A. E. Williams-Jones, J. J. Liu, S. F. Tombros, and N. J. Cook.
"Mineralogical, Fluid Inclusion, and Multiple Isotope (H-O-S-Pb) Constraints on the Genesis of the Sandaowanzi Epithermal Au-Ag-Te Deposit, Ne China."
Economic Geology 113, no. 6 (Sep 2018): 1359-82. http://dx.doi.org/10.5382/econgeo.2018.4595.

Au-Ag deposits are relatively rare in China, although several deposits, including Sandaowanzi (Tran et al. 2008), Guilaizhuang (Hu et al. 2006), and Dashuigou (Mao et al. 1995), fit this description. The Sandaowanzi deposit has a total reserve of ≥28 tonnes Au and an average grade of 15 g/t. Mining began at Sandaowanzi in 2006, and ≥20 tonnes of gold have been recovered to date. The deposit has attracted broad attention for two reasons: (1) it is the first example of a gold deposit in NE China, in which >95% of the gold is present as coarse-grained tellurides (Tran et al. 2008); and (2) it contains bonanza Au- and Ag-telluride ores, with grades of Au, Ag, and Te up to 35,000, 25,000 and 30,000 g/t, respectively.

The Sandaowanzi deposit is located in the northeastern segment of the Great Hinggan Range Metallogenic Belt, northeastern China (Fig. 1a), which hosts Fe±Sn skarns, Cu±Mo porphyry and epithermal Au±Ag deposits (Zhai et al. 2014, 2017a), all of which are related to a 140-110 Ma magmatic event (Mao et al. 2003, 2011; Wu et al. 2011; Zhai et al. 2017b, Fig. 1b). Although previous studies of the deposit, mostly published in Chinese, have addressed its geology (Wu ZY et al. 2005; Liu and Lu 2006; Tran et al. 2008; Lu et al. 2009a), mineralogy (Lu et al. 2009b; Han et al. 2011; Xu et al. 2011, 2012; Zhai et al. 2013; Zhai and Liu 2014; Liu et al. 2017), geochronology and tectonic setting (Chen and Sun 2011; Liu et al. 2011; Zhai et al. 2015; Gao et al. 2017; Wang et al. 2017), geophysics (Kong et al. 2006), stable isotope geochemistry (S, H, O) (Lu et al. 2005; Liu et al. 2013) and fluid inclusions (Zhao et al. 2010; Yu et al. 2012; Chen et al. 2012), issues related to fluid source, physicochemical conditions, and precipitation mechanisms remain unresolved and greatly debated. For example, Lu et al. (2005) considered that meteoric water was the dominant component of the hydrothermal fluid, whereas Liu and Lu (2006) concluded that the fluid system was dominantly magmatic. Zhao et al. (2010) argued that the ore fluid was a mixture of magmatic and meteoric fluids. Most recently, Zhai et al. (2015) have proposed that a significant proportion of mantle-derived fluid was added to the ore fluid and contributed to formation of the gold ore.

In this contribution, previously published data are briefly summarized, and new results of mineralogical, stable (O, H, and S) and Pb isotope and fluid inclusion analyses are presented. This integrated fluid inclusion and isotope geochemical study is based on a suite of representative samples from the different mineralization stages, ore types and depths in the hydrothermal system. These new data, in combination with physicochemical modeling, provide new insights into the

Zhai, D. G., A. E. Williams-Jones, J. J. Liu, S. F. Tombros, and N. J. Cook.
"Mineralogical, Fluid Inclusion, and Multiple Isotope (H-O-S-Pb) Constraints on the Genesis of the Sandaowanzi Epithermal Au-Ag-Te Deposit, Ne China."
Economic Geology 113, no. 6 (Sep 2018): 1359-82. http://dx.doi.org/10.5382/econgeo.2018.4595.

origin of the ore fluids and metals, and the mechanisms of Au-Ag telluride deposition. They should, therefore, also help guide genetic interpretation of the genesis of other large epithermal Au-Ag-Te deposits in comparable geological settings elsewhere.

Geological framework

Geology of the Great Hinggan Range

The Great Hinggan Range (GHR) was the product of closure of the Mongol-Okhotsk Ocean (160 Ma), which separated the North China Craton from the Siberian Craton (Fan et al. 2003; Wang et al. 2006; Fig 1a). This coincided with subduction of the oceanic Pacific and Izanagi plates beneath the continental Eurasian Plate (Wang et al. 2006; Wilde 2015); the GHR evolved through collision, which was followed by lithospheric thinning that was probably related to extensional detachment of core complexes (Pirajno 2013). These geotectonic processes resulted in formation of a Late Jurassic to Early Cretaceous, WNW-trending, intracontinental rift zone (Liu et al. 2011).

A distinctive feature of the GHR Metallogenic Belt was the development of a Permian metamorphic core complex (Niu et al. 2006), facilitated by intracontinental rifting, which was intruded by numerous A- and I-type granitoids during three discrete episodes of plutonism (Wu et al. 2002). A Late Permian (~270 to 250 Ma) episode was characterized by the emplacement of early calc-alkaline, I-type plutons (diorites, tonalites and granodiorites and late A-type syenites). This was followed by Triassic to Jurassic (~220 to 150 Ma) intrusion of highly fractionated, I- and A-type granodiorites, monzogranites, syenogranites and granites, including the Sandaowanzi monzogranite. The latest episode was characterized by the emplacement of Cretaceous (~130 to 120 Ma) I-type granodiorites, monzogranites, syenites and A-type granites (Wu FY et al. 2005). Compilations of available geochronological data for the igneous belt in NE China have demonstrated that the granitic rocks mainly formed in the Jurassic (~180 to 150 Ma) or Early Cretaceous (~130 to 120 Ma) (Wu FY et al. 2005). Widespread intrusion of Early Cretaceous granites coincided with regional delamination and lithospheric thinning (Wang et al. 2006; Zhang et al. 2008).

In the northeastern part of the GHR, the intrusions were contemporaneous with the formation of two major types of hydrothermal ore deposits, porphyry Cu±Mo deposits such as Duobaoshan and

Zhai, D. G., A. E. Williams-Jones, J. J. Liu, S. F. Tombros, and N. J. Cook.
"Mineralogical, Fluid Inclusion, and Multiple Isotope (H-O-S-Pb) Constraints on the Genesis of the Sandaowanzi Epithermal Au-Ag-Te Deposit, Ne China."
Economic Geology 113, no. 6 (Sep 2018): 1359-82. http://dx.doi.org/10.5382/econgeo.2018.4595.

Tongshan, and epithermal Au-Ag±Te deposits such as Sandaowanzi and Beidagou (Fig. 1b). There is no genetic relationship between the porphyry and epithermal deposits, as the porphyry systems formed much earlier (Paleozoic) than the epithermal deposits (Mesozoic), which have been interpreted to be related to oblique subduction and regional extension (Goldfarb et al. 2014).

Geology of the Sandaowanzi deposit

Volcanic rocks are widespread in the Sandaowanzi ore district (Fig. 1c), where they overlie the Sandaowanzi pluton. They are divided into two units, a lower Longjiang Formation, and an upper Guanghua Formation (Lu et al. 2005; Wang et al. 2006, Fig. 1c). The Longjiang Formation, which covers 80% of the ore district, is composed of basaltic trachyandesites overlain by continental flood basalts (Lu et al. 2009a). The former includes varieties of basalt, trachyte and andesite, with intercalations of andesitic breccias, rhyolite and tuff (Fan et al. 2003; Lu et al. 2005). Compositions of the latter vary from alkaline in the north to subalkaline in the south (Liu et al. 2011). Based on results of U-Pb age determinations for zircon in the trachyandesite, the Longjiang Formation was emplaced between 122 ± 1 and 124 ± 1 Ma (Cheng et al. 2017; Gao et al. 2017). The Guanghua Formation, which occurs mainly in the northeastern part of the deposit (Fig. 1c), is composed of rhyolite, perlite, tuff breccias, and tuffs (Fan et al. 2003; Lu et al. 2005). Zircon U-Pb ages for the rhyolite range from 125 ± 2 to 122 ± 1 Ma (Liu et al. 2011; Gao et al. 2017). The Sandaowanzi pluton, which is located in the southeastern part of the ore district (Fig. 1c), is a monzogranite with a zircon U-Pb age of 182 ± 1 Ma (Zhai et al. 2015). Numerous N-trending, mafic, syenitic, dioritic to granitic sills and dikes intrude the main granitoid body, the Longjiang volcanic rocks, and in rare cases also the mineralized veins (Fig. 2). These dikes have widths up to several meters, and ages of between 118 ± 1 and 115 ± 1 Ma (Liu et al. 2011; Zhao et al. 2013). A large volume of Quaternary gravels, which host placer gold orebodies, occur in river valleys to the west of the quartz vein orebodies (Fig. 2). These placers are interpreted to be weathering products of the Sandaowanzi veins (Zhai et al. 2013).

The distribution of the regional and local volcanic rocks is controlled mainly by NE-NNE-oriented fault-bounded basins (Liu et al. 2013), whereas the Sandaowanzi Au- and

Zhai, D. G., A. E. Williams-Jones, J. J. Liu, S. F. Tombros, and N. J. Cook.
"Mineralogical, Fluid Inclusion, and Multiple Isotope (H-O-S-Pb) Constraints on the Genesis of the Sandaowanzi Epithermal Au-Ag-Te Deposit, Ne China."
Economic Geology 113, no. 6 (Sep 2018): 1359-82. http://dx.doi.org/10.5382/econgeo.2018.4595.

telluride-bearing quartz veins represent the filling of NW-oriented faults (Lu et al. 2005). These faults typically strike of 120-300 m, and have a width of 1-10 m.

The Sandaowanzi vein system

The Sandaowanzi quartz vein system and associated Au-Ag-Te ores are hosted mainly in trachyandesites and andesitic breccias, and to a lesser extent, in andesites and trachytes of the Longjiang Formation (Figs. 1c and 2). Seven major high-grade quartz veins and thirteen minor, subparallel, steeply dipping, quartz veins and extensive stockworks were identified during geochemical surveys (Liu and Lu 2006). These veins extend vertically for as much as 700 m, and their maximum widths vary from ~3 to ~15 m and average ~6 m (Figs. 2 and 3).

Three different mineralized zones referred to as I, II and III, with lengths of ~500, ~200 and 400 m and widths of X, Y and Z m, respectively, have been discovered (Liu and Lu 2006). They contain 15 steeply dipping (55-75°) Au-Ag-Te orebodies, most of which consist of single (multiply filled, veins and veinlets) quartz veins (Fig. 3). Several of the orebodies, however, comprise low-grade disseminations hosted by intensely silicified andesitic breccias and trachyandesites (Fig. 3). A few oxidized trachyandesite-hosted mineralized veins were observed in outcrops in which the trachyandesite was altered and brecciated (Fig. 4a and b).

This study focused mainly on the number I orebody (Fig. 3), because it is the only one currently being mined underground. This Au-bearing quartz vein varies in width from ~0.8 to ~14.3 m, extends up to 300 m down dip (58-77° NW), and strikes to the NNW (Fig. 3). The mineralization is in the form of micro-stockworks of almost pure coarse-grained telluride hosted by vein quartz. Macroscopically, the Au- and Ag-tellurides occur as massive veinlets or disseminated aggregates intergrown with chalcopyrite within colloform layers. Two ore shoots were distinguished. The first is located between the +270 and +210 m mining-levels, and has grades ranging from ~77 to 543 g/t Au (averaging ~215 g/t), whereas the second occurs between the +170 and +130 m mining-levels and has unusually high contents of Au (~31 to 35,000 g/t; average grade 791 g/t) and maximum Ag and Te grades of 25,000 and 30,000 g/t, respectively. These ore shoots were first identified at the +170 m mining-level but the highest grades are located at the +130 m mining-level where a veinlet ~50 cm wide consisting almost entirely of Au- and Ag-tellurides was identified. The high grade

Zhai, D. G., A. E. Williams-Jones, J. J. Liu, S. F. Tombros, and N. J. Cook.
"Mineralogical, Fluid Inclusion, and Multiple Isotope (H-O-S-Pb) Constraints on the Genesis of the Sandaowanzi Epithermal Au-Ag-Te Deposit, Ne China."
Economic Geology 113, no. 6 (Sep 2018): 1359-82. http://dx.doi.org/10.5382/econgeo.2018.4595.

ores, with Au grades up to 324 g/t (average of 17 g/t), occur almost exclusively between the + 300 and + 90 m mining-levels (Lu et al. 2009b), and are commonly surrounded by the disseminated ores in the +320 to +50 m mining-levels. The disseminated ore has a variable Au grade (~0.4 to ~85 g/t with an average of ~9 g/t). From the +50 to +10 m mining-levels, low-grade disseminated ores (averaging ~1.1 g/t) are dominant. The disseminated ores contain chalcopyrite and minor sphalerite, pyrite, tetrahedrite and galena intergrown with Au- and Ag-tellurides.,

Crustification is common in the quartz veins, particularly in the veins comprising them that are wider than 5 cm. Four types of vein material (Type A to D; Fig. 4c-f) have been distinguished based on mineralogy, grain size and texture. The general sequence of vein crustification, from the margins of the vein to the center, is: (i) fine-grained milky quartz ± illite, with colloform banding, comb, cockade and open space filling by clear quartz (>90 vol.%) and abundant angular fragments of altered and pyritic trachyandesite (Type A) (Fig. 4c-f); (ii) fine- to medium-grained grey quartz-illite with minor colloform and vug textures (>70 vol.%) and abundant poorly-sorted variably-sized fragments of milky quartz and rare altered trachyandesite (>10 vol.%) (Fig. 4e), containing substantial sulfide and minor telluride mineralization (Fig. 4c-e) (Type B); (iii) medium-grained clear quartz ± fine-grained adularia, with crack-seal textures (>50 vol.%) and abundant aggregates, masses or isolated crystals of telluride (Type C) (Fig. 4c-e); and (iv) coarse-grained white quartz (<70 vol.%) and calcite (<30 vol.%) ± chlorite or calcite veinlets containing native gold (Type D) (Fig. 4d, f). Isolated veinlets of Types B, C and D commonly accompany the major crustiform veins. The milky, grey and white quartz veins are locally cut by clear quartz vein, mostly reflecting multiple episodes of quartz vein formation (Fig. 4f).

Hydrothermal alteration

The major gold-bearing quartz veins are hosted by intensely pyritized and silicified andesitic breccias and trachyandesites. Locally the pyritized trachyandesites have been incorporated in the quartz veins as isolated fragments or breccias (Fig. 4f). In addition, the quartz veins are accompanied by well-developed alteration halos comprising an inner silicic zone, two intermediate zones containing quartz-illite-sericite and quartz-adularia, and an outer zone of quartz-calcite-kaolinite-chlorite, all of which are accompanied by abundant pyrite. These minerals

Zhai, D. G., A. E. Williams-Jones, J. J. Liu, S. F. Tombros, and N. J. Cook.
"Mineralogical, Fluid Inclusion, and Multiple Isotope (H-O-S-Pb) Constraints on the Genesis of the Sandaowanzi Epithermal Au-Ag-Te Deposit, Ne China."
Economic Geology 113, no. 6 (Sep 2018): 1359-82. http://dx.doi.org/10.5382/econgeo.2018.4595.

replaced orthoclase, albite, anorthite, biotite, muscovite, hornblende, and tremolite. The alteration is distributed asymmetrically around the veins and locally is discontinuous, but is generally thickest adjacent to the widest veins. Furthermore, the different alteration assemblages may be overlapped and thus superimposed, although commonly, the youngest alteration is characterized by illite and grey quartz. Silicic alteration is observed near milky quartz veins. Micro-stockworks of silica-veinlets filled with crypto- to micro-crystalline milky quartz and chalcedony cut the host andesitic breccias and trachyandesites. Based on the alteration mineral assemblage, the deposit is classified as an adularia-sericite type epithermal deposit (Heald et al. 1987).

Sampling and analytical methods

Approximately 80 samples were collected from the different mining levels (+170 to +50 m). The samples include crustified quartz veins of the Number I ore body from Type A to D vein material, pyrite samples from alteration zones, and whole-rock samples from the host trachyandesites, basaltic dikes, and the Sandaowanzi monzogranite. Polished and doubly-polished thin sections were examined with reflected and transmitted light microscopes. Primary ore textures were identified using a Hitachi Scanning Electron Microscope equipped with an Oxford IE350 energy-dispersive detector at the China University of Geosciences, Beijing (CUGB). Mineral compositions were determined with a JEOL 8230 Superprobe, equipped with wavelength- and energy-dispersive and back-scattered detectors at the Chinese Academy of Geological Sciences (CAGS), Beijing. The operating conditions were a 15 kV acceleration voltage, a 20 nA beam current and a 20 s counting time for all elements. Natural and synthetic mineral standards of chalcopyrite, pyrite, sphalerite, galena, CoNiAs, SnO_2, MnTi and native Ag, Sb, Au, Se, Te, and Cd were used for calibration. ZAF corrections were made with proprietary JEOL software. The analytical results (sulfides, sulfosalts and tellurides) are presented in Table 1.

Prior to microthermometric analyses, the internal zoning of quartz was examined using a cathodoluminescence (CL) spectrometer (Garton Mono CL3+) attached to a Quanta 200F ESEM at Peking University. The operating conditions were a 15 kV acceleration voltage and a 120 nA beam current, coupled to a 45-s scanning time. Microthermometric measurements of fluid inclusions were performed on a LINKAM MDSG600 heating-freezing stage mounted on a ZEISS microscope in the

Zhai, D. G., A. E. Williams-Jones, J. J. Liu, S. F. Tombros, and N. J. Cook.
"Mineralogical, Fluid Inclusion, and Multiple Isotope (H-O-S-Pb) Constraints on the Genesis of the Sandaowanzi Epithermal Au-Ag-Te Deposit, Ne China."
Economic Geology 113, no. 6 (Sep 2018): 1359-82. http://dx.doi.org/10.5382/econgeo.2018.4595.

School of Earth Sciences and Resources, CUGB. Most analyzed quartz crystals were directly in contact with sulfides, tellurides and native gold. The temperature range for the stage varied from -196 to +600 °C. The LINKAM stage was calibrated at -56.6 °C, +0.0 °C, and +374.1 °C with synthetic fluid inclusions. Measurements were accurate to within ± 0.1 ºC below zero Celsius, whereas at higher temperature the error ranged up to ± 1 ºC. Freezing-heating rates were between 0.2 and 5 °C/min. When approaching a phase transition, however, the rate was dropped to 0.1-0.5 °C/min. The microthermometric data were reduced using FLINCOR software (Brown 1989) and are summarized in Table 2.

Fluid inclusion laser Raman spectroscopic analysis was carried out in the Beijing Research Institute of Uranium Geology, Beijing, China, using a Renishaw RM-2000 Raman microscope. This instrument records peaks in the range of 100-4000 cm^{-1} full-band with a resolution of 1-2 cm^{-1}; the laser beam spot size was about 1 μm. The inclusions were analyzed for the common gases, monoatomic and polyatomic ions and molecules. Analyses of the gas composition of the bulk included fluid were carried out at CAGS using a crusher attached to a gas chromatograph following the method described by Salvi and Williams-Jones (1997). The composition of the liquid was analyzed using the crush-leach method and a Shimadzu HIC-SP Super ion chromatograph. These analyses were restricted to samples dominated by a single generation of fluid inclusions. Reference materials for gaseous analysis were synthetic fluid inclusions and liquids selected from the national standard materials study center. The results of the bulk analyses are presented in Table 3.

Stable isotope analyses were conducted on milky, grey, clear and white quartz vein material (Types A to D), sulfides (chalcopyrite and pyrite) and host trachyandesites and monzogranites. All minerals selected were handpicked and checked under a binocular microscope to ensure a purity of >98%. Isotopic compositions of oxygen and hydrogen (quartz) and sulfur (sulfides) were analyzed using a MAT-253 stable isotope ratio mass spectrometer (CAGS). Oxygen was extracted for analysis using the BrF_5 technique (Clayton and Mayeda 1963) and hydrogen from H_2O released from fluid inclusions (Coleman et al. 1982). Sulfur was released as SO_2 (Fritz et al. 1974). The isotopic ratios are reported in standard δ notation (‰) relative to SMOW for oxygen and hydrogen, and CDT for sulfur. The analytical precision was better than ± 0.2 ‰ for $\delta^{18}O$, ± 2 ‰ for δD, and ±

Zhai, D. G., A. E. Williams-Jones, J. J. Liu, S. F. Tombros, and N. J. Cook.
"Mineralogical, Fluid Inclusion, and Multiple Isotope (H-O-S-Pb) Constraints on the Genesis of the Sandaowanzi Epithermal Au-Ag-Te Deposit, Ne China."
Economic Geology 113, no. 6 (Sep 2018): 1359-82. http://dx.doi.org/10.5382/econgeo.2018.4595.

0.2 ‰ for $\delta^{34}S$. Results of the sulfur isotope analyses are given in Table 4, and of the D and O isotope analyses in Table 5.

Pyrite in altered trachyandesites, and whole-rock samples of the Sandaowanzi monzogranites and host trachyandesites were analyzed for their lead isotope composition. The analyses were carried out at CAGS using an England Nu Plasma, high-resolution, multi-collector inductively-coupled plasma mass spectrometer (MC-ICP-MS) and a standard from the National Bureau of Standards (NBS981). Long-term repeated measurements of the Pb isotopic ratios of standard NBS981 yielded $^{206}Pb/^{204}Pb$ = 16.9397 ± 0.0111, $^{207}Pb/^{204}Pb$ = 15.4974 ± 0.0089, and $^{208}Pb/^{204}Pb$ = 36.7147 ± 0.0262 (all errors are reported at ±2σ). The lead isotope data are given in Table 6.

Results

Mineralogy

More than 35 sulfide, sulfosalt, telluride and gangue minerals have been identified at Sandaowanzi. The ore and alteration minerals have been classified into four paragenetic stages based on their textural relationships, the nature of the quartz and partly the accompanying alteration minerals (Zhai and Liu 2014). Stage I mainly contains milky quartz, Stage II is composed of grey quartz and illite, Stage III comprises clear quartz with an alteration assemblage of quartz and adularia, and Stage IV consists of white quartz, calcite and kaolinite with chlorite. These stages correspond to the Type A to Type D vein materials referred to earlier.

Stage I is dominated by intergrowths of milky quartz, pyrite and rare pyrrhotite (reported by Wu ZY et al. 2005; Liu and Lu 2006). In the milky quartz veins, pyrite is typically euhedral, and was replaced or cemented by other sulfides (mainly chalcopyrite) and/or tellurides in Stages II and III. Stage II is dominated by massive aggregates of sulfides, sulfosalts, minor tellurides and native gold, and is developed mainly in the disseminated ores. Chalcopyrite is very common and aggregates of sphalerite and galena are also observed. Sulfides (i.e., chalcopyrite) and sulfosalts (i.e., tennantite) commonly coexist with minor tellurides, i.e., petzite (Ag_3AuTe_2), calaverite ($AuTe_2$), altaite (PbTe) and hessite (Ag_2Te) in this stage (Fig. 5a).

Zhai, D. G., A. E. Williams-Jones, J. J. Liu, S. F. Tombros, and N. J. Cook.
"Mineralogical, Fluid Inclusion, and Multiple Isotope (H-O-S-Pb) Constraints on the Genesis of the Sandaowanzi Epithermal Au-Ag-Te Deposit, Ne China."
Economic Geology 113, no. 6 (Sep 2018): 1359-82. http://dx.doi.org/10.5382/econgeo.2018.4595.

Stage III is dominated by abundant tellurides (≥95 vol.%), which replaced Stage II sulfides and/or tellurides (Figs. 4c-f and 5b-i). Subhedral altaite is commonly associated with petzite, hessite, sylvanite [$(Au,Ag)_2Te_4$] and krennerite [$(Au,Ag)Te_2$] (Fig. 5b, d, h). Assemblages of hessite-petzite, hessite-stützite ($Ag_{5-x}Te_3$), and hessite-empressite (AgTe)-petzite (Fig. 5c-i) are very common. Gold-bearing telluride assemblages, containing krennerite, sylvanite, calaverite, and traces of native gold (Fig. 5e-h) are also present in this stage. Sulfides (i.e., chalcopyrite and sphalerite) and sulfosalts (i.e., tetrahedrite) (≤5 vol.%) are present in minor amounts (Fig. 5c-f, h). Stage III ended with precipitation of Cu-Zn and Pb-Zn-Cu alloys (Zhai and Liu 2014), which occur as isolated grains in a clear quartz matrix. Finally, Stage IV is dominated by native gold, hematite and goethite. Native gold appears as isolated grains in quartz or as veinlets crosscutting Stage III petzite and hessite (Fig. 5d, e).

Fluid inclusions

Fluid inclusions are common in quartz and were classified as primary, pseudo-secondary or secondary with the assistance of cathodoluminesence. Scanning electron microscope and cathodoluminesence images show that a high proportion of the quartz crystals experienced oscillatory zoning (Fig. 6a). The early quartz displaying oscillatory zoning was commonly overprinted by later quartz that also displays oscillatory zoning (Fig. 6b-d). In places, however, the later quartz filled fractures in the early quartz displaying oscillatory zoning and is relatively homogeneous (Fig. 6e, f). This study reports microthermometric data for ten samples covering mineralization Stages I to IV. Primary inclusions were identified mainly on the basis of their occurrence along growth zones (Fig. 7a, b) and only such inclusions with no signs of necking were used in the microthermometric study. Each cluster or set of inclusions along a growth zone was considered to represent a separate fluid inclusion assemblage (FIA), which was carefully documented and measured. The primary inclusions are typically 5-15 μm in diameter and are either spherical, elliptical or irregular in shape (Fig. 7a-g). They are found in quartz from each of the four mineralization stages. Numerous secondary inclusions and a small population of pseudosecondary inclusions were also observed.

Zhai, D. G., A. E. Williams-Jones, J. J. Liu, S. F. Tombros, and N. J. Cook.
"Mineralogical, Fluid Inclusion, and Multiple Isotope (H-O-S-Pb) Constraints on the Genesis of the Sandaowanzi Epithermal Au-Ag-Te Deposit, Ne China."
Economic Geology 113, no. 6 (Sep 2018): 1359-82. http://dx.doi.org/10.5382/econgeo.2018.4595.

At room temperature, three types of fluid inclusions were recognized: (i) L-V inclusions, which consist of aqueous liquid + vapor with a dominant liquid phase (V/L+V = 10-20 vol.%, Fig. 7a-d, g); (ii) V-L inclusions consisting of aqueous liquid + vapor with a dominant vapor phase (V/L+V = 60-80 vol.%); and (iii) L-V-S inclusions consisting of aqueous liquid + vapor + solid (Fig. 7e, f). The solids in inclusions almost invariably show inconsistent volume ratios with the other phases, indicating that they are accidentally trapped solids. Significantly, liquid-rich (L-V) and vapor-rich (V-L) inclusions are observed coexisting in single growth zones in quartz from each of the mineralization stages, providing petrographic evidence that the fluid boiled during each of these stages (Fig. 7c, d). No CO_2-rich fluid inclusions or inclusions that developed clathrates on cooling were observed.

Liquid-vapor homogenization temperatures were determined for 364 fluid inclusions, including 60 FIAs for both homogenization and final ice melting temperatures (Fig. 9, Table 2). Fluid inclusion assemblages of L-V and V-L types in stage I, II, III and IV veins have mean liquid-vapor homogenization temperatures of 330 ºC, 280 ºC, 240 ºC and 200 ºC, respectively (Fig. 8). The final ice melting temperature (T_m) for the different FIAs ranged from -11.6 to -0.3 ºC (Table 5), corresponding to a salinity range from 0.5 to 15.6 wt.% NaCl equiv. (salinity was estimated from the equations of Brown and Lamb 1989). Most of the FIAs from the different mineralized stages are characterized by a salinity lower than 6.0 wt.% NaCl equiv. (Fig. 9). The exceptions are those from Stage III, some of which report relatively high values (as high as 15.6 wt.% NaCl equiv.). Fluid inclusion assemblages of the four mineralized stages have a median salinity of 1.5, 2.2, 4.7 and 2.2 wt.% NaCl equiv., respectively (Table 2; Fig. 8). In summary, the homogenization temperature decreased from an excess of 300 ºC during Stage 1 to less than 200 ºC during Stage IV (Fig. 9). The salinity, in contrast, increased from values during Stage I that were < 4 wt% NaCl equiv. to values during Stage III that locally reached nearly 16 wt% NaCl equiv. and then decreased to values during Stage IV that were similar to or slightly less than those of Stage 1 (Fig. 9).

Gas chromatographic analyses of the bulk inclusion fluid indicate that CO_2 was the principal incondensable gas and was accompanied by trace proportions of CH_4 (Table 3). Ion chromatographic analyses indicate that Ca^{2+} was the dominant cation except in Stage IV for which K^+ was the dominant cation. Significantly K^+ was the next most cation for all other stages and for

Zhai, D. G., A. E. Williams-Jones, J. J. Liu, S. F. Tombros, and N. J. Cook.
"Mineralogical, Fluid Inclusion, and Multiple Isotope (H-O-S-Pb) Constraints on the Genesis of the Sandaowanzi Epithermal Au-Ag-Te Deposit, Ne China."
Economic Geology 113, no. 6 (Sep 2018): 1359-82. http://dx.doi.org/10.5382/econgeo.2018.4595.

all stages Na^{+} only ranked third (Table 3). Sulfate was the dominant anion followed by Cl- and F-. The dominant cation is Ca^{+2} and the dominant anion is SO_4^{-2} (Table 3).

Stable isotopes

Sulfur isotopic compositions

Sulfur isotope analyses were conducted on pyrite samples from alteration zones and quartz veins, and chalcopyrite samples from quartz veins (Table 4). The measured $\delta^{34}S_{CDT}$ values of pyrite from the altered rocks and Stage II mineralization range from -0.5 to +0.9 and -0.9 to +0.6 ‰, respectively, whereas those of chalcopyrite from Stages II and III are -1.8 and -2.2 ‰, respectively (Table 4). Temperatures ranging from 267° to 318 °C (average of 292 ± 5°C) for Stage II were calculated for coexisting pyrite and chalcopyrite in the veins using the equations of Ohmoto and Lasaga (1982). The calculated values of $\delta^{34}S_{H2S}$ for the mineralizing fluid in equilibrium with these minerals range from -2.2 to -0.2 ‰ assuming the temperatures for each stage predicted by the fluid inclusion homogenization temperatures (Table 4).

Hydrogen and oxygen isotopic compositions

The $\delta^{18}O$ and δD values for the Stage I, II, III and IV quartz veins are -2.5 ‰ and -123 ‰, -1.9 to -0.3 ‰ and -116 to -98 ‰, -3.9 to -0.3 ‰ and -123 to -96 ‰, -3.5 to -2.6 ‰ and -127 to -109 ‰, respectively (Table 5). Based on their average homogenization temperatures, the calculated $\delta^{18}O_{H2O}$ values of the mineralizing fluids are -10.6 ‰ (Stage I), -10.1 to -8.3 ‰ (Stage II), -12.9 to -9.8 ‰ (Stage III) and -13.6 to -7.6 ‰ (Stage IV) (Table 5); the δD values are -123 ‰ (Stage I), -116 to -98 ‰ (Stage II), -123 to -96 ‰ (Stage III) and -127 to -109 ‰ (Stage IV) (Table 5). The whole-rock $\delta^{18}O$ isotopic values of the host trachyandesite and the Sandaowanzi monzogranite range from -4.4 to -1.4 ‰ and +1.5 to +3.1 ‰, respectively (Table 5).

Lead isotopes

Lead isotope data were obtained for pyrite in trachyandesites and whole-rock samples of Sandaowanzi monzogranite and host trachyandesite (Table 6). The $^{206}Pb/^{204}Pb$ (18.2093 to 18.8377 ± 0.0008), $^{207}Pb/^{204}Pb$ (15.5409 to 15.6255 ± 0.0008), $^{208}Pb/^{204}Pb$ (38.0901 to 38.6944 ± 0.0020), $^{208}Pb/^{206}Pb$ (2.0541 to 2.0994 ± 0.0001) and $^{207}Pb/^{206}Pb$ (0.8274 to 0.8577 ± 0.0001) ratios reveal homogenous compositions. On the $^{206}Pb/^{204}Pb$ versus $^{207}Pb/^{204}Pb$ uranogenic and $^{206}Pb/^{204}Pb$ versus

Zhai, D. G., A. E. Williams-Jones, J. J. Liu, S. F. Tombros, and N. J. Cook.
"Mineralogical, Fluid Inclusion, and Multiple Isotope (H-O-S-Pb) Constraints on the Genesis of the Sandaowanzi Epithermal Au-Ag-Te Deposit, Ne China."
Economic Geology 113, no. 6 (Sep 2018): 1359-82. http://dx.doi.org/10.5382/econgeo.2018.4595.

$^{208}Pb/^{204}Pb$ thorogenic plots, most pyrite and monzogranite samples plot on the global mantle growth curve (Fig. 11a, b; Zartman and Doe 1981). Two trachyandesite samples appear just above the global orogen growth plumbotectonic curve (Zartman and Doe 1981); one monzogranite sample plots between the mantle and orogen curves (Fig. 11a, b).

Discussion

Temperature-pressure conditions

The homogenization temperatures of fluid inclusions trapped in the different stage quartz veins demonstrate that milky quartz (Stage I) mainly formed at temperatures between 280º and 350ºC (average 330ºC), grey quartz (Stage II) from 240º to 320ºC (average 280ºC), clear quartz (Stage III) at 210º to 280ºC (average 240ºC), and white quartz (Stage IV) (post-telluride stage) from 150º to 220ºC (average 200ºC) (Fig. 8). An independent estimate of temperature is provided by the sulfur isotope data for pyrite and chalcopyrite in Stage II veins. These data indicate a temperature of 292 ºC which is only marginally higher than the average homogenization temperature for fluid inclusions in these veins. This suggests that any pressure correction for the latter data would be relatively minor. The temperatures (from 200º to 330ºC) reported above are slightly higher than those for most epithermal gold and silver deposits (they are mostly from 150º to 300ºC, Simmons et al. 2005 and references therein), although similar temperatures have been reported for some epithermal precious and base metal deposits (Bodnar et al. 2014).

As shown earlier, L-V inclusions coexisted with V-L inclusions in growth zones of quartz representing each of the mineralization stages, indicating that the fluid boiled throughout the mineralizing event. In order to constrain the pressure of ore deposition during different mineralizing stages, we calculated this pressure using the 'HOKIE FLINCS_H2O-NACL' spreadsheet of Steele-MacInnis et al. (2012) for a boiling fluid system. The results of these calculations show that pressure was highest during formation of Stage I veins, ranging from 150 to 200 bars. Assuming hydrostatic conditions (suggested by the nature of the veins) these pressures are equivalent to paleodepths of 1.5 to 2.0 km. These pressures and the corresponding depths are slightly higher and deeper, respectively, than those for most epithermal deposits (typically <150 bars and <1.5 km, Simmons et al. 2005). In contrast, the pressures for Stages II and III range from 80 to 160 bars and

Zhai, D. G., A. E. Williams-Jones, J. J. Liu, S. F. Tombros, and N. J. Cook.
"Mineralogical, Fluid Inclusion, and Multiple Isotope (H-O-S-Pb) Constraints on the Genesis of the Sandaowanzi Epithermal Au-Ag-Te Deposit, Ne China."
Economic Geology 113, no. 6 (Sep 2018): 1359-82. http://dx.doi.org/10.5382/econgeo.2018.4595.

from 70 to 130 bars, respectively. These results predict that the depths were 0.8 to 1.6 km and 0.7 to 1.3 km for Stage II and III veins, respectively. The late stage gold-quartz-calcite veins formed temperatures between 150° and 220°C and pressures corresponding to predicted depths of 0.2 to 0.8 km assuming hydrostatic conditions. As the paleodepth would have been constant for all mineralizing stages, it seems likely that the pressure was somewhat greater than hydrostatic during the early stages and approached hydrostatic during Stage IV, suggesting that the vein system was probably emplaced at a depth significantly less than 1 km.

In summary, based on fluid inclusion microthermometry, gold-telluride mineralization at Sandaowanzi was deposited at a temperature range of 280º to 210°C under near hydrostatic conditions at a depth of < 1 km; the native gold was deposited later at a temperature of 220° to 150°C.

Fluid Composition and Evolution

The fluid salinity (mostly <6 wt.% NaCl equiv.) is in the upper part of the range for low-sulfidation epithermal gold deposits (commonly <5 wt.% NaCl equiv., Simmons et al. 2005; Bodnar et al. 2014). However, this salinity is consistent with that of telluride-rich low-sulfidation epithermal deposits, which typically have slightly higher salinity (commonly 5-10% NaCl equiv., Ahmad et al. 1987; Saunders 1991; Zhang and Spry 1994; Tombros et al. 2008). The elevated salinity was mostly due mainly to intense boiling of the fluid, which concentrated the dissolved salts. Indeed, the observed increase in the average salinity from Stages I to III (average in 1.5, 2.2, 4.7 wt.% NaCl equiv., respectively) is consistent with this hypothesis (also see Fig. 9). The return to low salinity during Stage IV (Fig. 9), which represents the waning coolest stage of the system, could reflect an incursion of meteoric water, although evidence for this is not apparent in our data .

Source of metallic and hydrothermal components of the ore fluids

The calculated $\delta^{34}S_{H2S}$ values of the hydrothermal fluids range from -4.8 to +2.7 ‰ with most of the data being between -2.5 and +0.5 ‰ (Fig. 10). These $\delta^{34}S_{H2S}$ values indicate a magmatic source for the sulfur and are interpreted to mostly reflect leaching of sulfur from the host volcanic rocks. The $^{206}Pb/^{204}Pb$ vs. $^{207}Pb/^{204}Pb$ uranogenic and $^{206}Pb/^{204}Pb$ vs. $^{208}Pb/^{204}Pb$ thorogenic data (Fig. 11)

Zhai, D. G., A. E. Williams-Jones, J. J. Liu, S. F. Tombros, and N. J. Cook.
"Mineralogical, Fluid Inclusion, and Multiple Isotope (H-O-S-Pb) Constraints on the Genesis of the Sandaowanzi Epithermal Au-Ag-Te Deposit, Ne China."
Economic Geology 113, no. 6 (Sep 2018): 1359-82. http://dx.doi.org/10.5382/econgeo.2018.4595.

411 reveal that the lead was of mantle or magmatic origin, and it is therefore likely that it also was
412 inherited from the host volcanic rocks during fluid-rock interaction. These rocks have a mantle
413 origin and probably formed as a result of regional asthenospheric upwelling in NE China (Fan et al.
414 2003; Wang et al. 2006).

415 The $\delta^{18}O_{H2O}$ values (-13.6 to -7.6‰) and δD_{H2O} values of the ore fluid calculated to have been in
416 equilibrium with vein quartz are consistent with a dominantly meteoric fluid that underwent modest
417 interaction with the host rocks (Fig. 12). This interpretation is supported by analyses of the
418 composition of the fluid, which show that the dominant cation is Ca^{2+} rather than Na^{+} and that the
419 dominant anion is a sulfur species rather than Cl^{-} (Table 3). It also agrees with the findings for other
420 low sulfidation epithermal deposits including those are dominated by telluride minerals (Shelton et
421 al. 1990; Zhang and Spry 1994).

422

423 ***Genetic association between alkaline magmatism and Au-Te mineralization***

424 It is significant that the Sandaowanzi gold-telluride veins are hosted by alkaline igneous rocks, as
425 this metallogenic association has attracted much attention due to a possible connection between the
426 magmatism and the mineralization (Jensen and Barton 2000; Sillitoe 2002). Indeed, numerous
427 studies of gold-telluride deposits have suggested that tellurium and gold in these deposits mostly
428 originated from the spatially and temporally associated alkaline magmas (e.g., Golden Sunlight,
429 Montana, Porter and Ripley 1985; Cripple Creek, Colorado, Thompson et al. 1985; Emperor, Fiji,
430 Ahmad et al. 1987; Porgera, Papua New Guinea, Richards 1990; Judith Mountains, Montana, Zhang
431 and Spry 1994). The economic importance of gold-telluride mineralization results from the fact that
432 some of these deposits are giants in terms of ore reserves (Ciobanu et al. 2006). A possible
433 explanation for this association is that it may reflect enrichment of tellurium in the lithospheric
434 mantle, possibly by sediment recycling (Jensen and Barton 2000). According to this explanation, the
435 tellurium is transported into the crust by the rift-related alkaline magmas that also originate in this
436 environment. Cooke and McPhail (2001) suggested that the generation of magmatic gases may also
437 be critical due to the likely transport of Te in the gas phase. It may therefore also be significant that
438 the available geochronological data show that the gold-telluride veins and their host alkaline

Zhai, D. G., A. E. Williams-Jones, J. J. Liu, S. F. Tombros, and N. J. Cook.
"Mineralogical, Fluid Inclusion, and Multiple Isotope (H-O-S-Pb) Constraints on the Genesis of the Sandaowanzi Epithermal Au-Ag-Te Deposit, Ne China."
Economic Geology 113, no. 6 (Sep 2018): 1359-82. http://dx.doi.org/10.5382/econgeo.2018.4595.

volcanic rocks at Sandaowanzi formed synchronously at ~120 Ma (Liu et al. 2011; Zhai et al. 2015; Wang et al. 2017).

Physicochemical conditions of alteration and ore mineral formation

The physicochemical conditions of alteration and ore mineral deposition, other than temperature and pressure, were interpreted from phase stability relationships using SUPCRT92 (Johnson et al. 1992) and the recently published extended database (Zimmer et al. 2016). The thermodynamic properties of the tellurides were compiled from McPhail (1995) and Tombros et al. (2010); all solids were considered to be ideal solutions.

Values of pH were calculated from the bulk composition of the fluid inclusions (Table 3), and from mineral equilibria in the system. Based on the presence of minor illite and the absence of K-feldspar in Stage I, the pH values for this stage are estimated to have ranged from 3.0 to 3.2 (Fig. 15a). Similarly, the alteration mineral assemblages of quartz-illite-sericite, quartz-adularia, and quartz-calcite-kaolinite-chlorite in Stages II, III and IV are interpreted to reflect pH values that ranged from 4.0 to 4.3 (Fig. 15b), 4.5 to 5.1 (Fig. 15c) and 5.9 to 6.0 (Fig. 15d), respectively. The presence of pyrite, chalcopyrite and minor tellurides (calaverite and altaite) and absence of pyrrhotite in Stage II (280°C) suggest $\log fS_2$ values of -12.1 to -9.2 (Fig. 16a). As the temperature dropped towards 240°C (Stage III), the coexistence of pyrite and chalcopyrite and abundant telluride formation required $\log fS_2$ values between -14.1 and -10.6 (Fig. 16b, Table 7). The presence of hessite and altaite in Stage III at 240 °C indicates that the $\log fTe_2$ values ranged from -11.6 to -8.1 (Fig. 16b). The maximum and minimum $\log fTe_2$ values for Stage II are based on the presence of calaverite ($\log fTe_2 \geqslant$-8.5) and altaite, the absence of native tellurium ($\log fTe_2 \leq$ -7.0) and presence of native gold. Likewise, $\log fTe_2$ values for Stage III are constrained by the widespread occurrence of calaverite-native Au ($\log fTe_2 \approx$ -9.8) and altaite, and the absence of native tellurium ($\log fTe_2 \leq$ -8.1) (Fig. 16a, b).

To constrain the various physicochemical parameters and evaluate possible ore deposition mechanisms (the next discussion section), the following reactions were considered:

$$AuAg_3Te_{2(s)} + Ag^+_{(aq)} = 2Ag_2Te_{(s)} + Au^+_{(aq)} \quad (1)$$

$$AuAg_3Te_{2(s)} = AuTe_{2(s)} + 3Ag_{(aq)} \quad (2)$$

Zhai, D. G., A. E. Williams-Jones, J. J. Liu, S. F. Tombros, and N. J. Cook.
"Mineralogical, Fluid Inclusion, and Multiple Isotope (H-O-S-Pb) Constraints on the Genesis of the Sandaowanzi Epithermal Au-Ag-Te Deposit, Ne China."
Economic Geology 113, no. 6 (Sep 2018): 1359-82. http://dx.doi.org/10.5382/econgeo.2018.4595.

$H_2Te_{(g)} = H_2Te_{(aq)} = H^+_{(aq)} + HTe^-_{(aq)}$ (3)

$0.5H_2O_{(l)} + Au(HS)^-_{2(aq)} = Au_{(s)} + 2HS^-_{(aq)} + H^+_{(aq)} + 0.25O_{2(g)}$ (4)

$H_2S_{(g)} = H_2S_{(aq)} = H^+_{(aq)} + HS^-_{(aq)}$ (5)

$2Ag(HS)^-_{2(aq)} + HTe^-_{(aq)} = 4HS^-_{(aq)} + Ag_2Te_{(s)} + H^+_{(aq)}$ (6)

$Au(HS)^-_{2(aq)} + 2HTe^-_{(aq)} + H^+_{(aq)} = 2HS^-_{(aq)} + AuTe_{2(s)} + 1.5H_{2(aq)}$ (7)

From the petzite-hessite and calaverite-petzite equilibria in Stage III, the $\log\alpha Au^+_{(aq)}/\alpha Ag^+_{(aq)}$ values in solution range were estimated to have been from -6.8 to -5.9 (Reactions 1 and 2). Using the bulk composition data for the gas phase in fluid inclusions (Table 3), equilibria involving the gas phases and the mineral equilibria, the $\Delta\log fO_2$ (HM) values were constrained to have been from -2.6 to -2.2 (Stage I), -2.1 to -1.0 (Stage II), -0.6 to -0.4 (Stage III) and +1.9 (Stage IV) (Table 7). Utilizing the same data, approach and relevant reactions (3 and 4), the $\log\alpha_{H2S(aq)}$, $\log f_{H2S(g)}$, $\log\alpha_{H2Te(aq)}$, $\log f_{H2Te(g)}$, $\log fH_2S_{(g)}/fSO_{2(g)}$ and $\log\alpha Au(HS)_2^-{}_{(aq)}$ values were also estimated for Stages I to IV (summarized in Table 7). Finally, based on the saturation in the fluid of pyrite, sphalerite, chalcopyrite and galena, $\log\alpha Fe^{++}_{(aq)}$, $\log\alpha Zn^{++}_{(aq)}$ and $\log\alpha Cu(HS)_2^{-}{}_{(aq)}$ values were also constrained.

Mechanisms of ore deposition

Deposition of calaverite and hessite from the ore fluids was likely controlled by Reactions 6 and 7 or possibly analogous reactions involving the species $Au(HS)^o$ and $Ag(HS)^o$, given the estimates of log fO_2 and pH. From these reactions, it is evident that deposition of these minerals depended heavily of the values of $aHS^-_{(aq)}$ and $aHTe^-_{(aq)}$, although changing pH, and in the case of Reaction 7 afH_2 may also have played a role.

Given the importance of boiling in the system, it is attractive to propose that boiling was responsible for ore formation, as has been proposed for many adularia-sericite or low sulfidation epithermal systems (add references). As is evident from Figure 17, however, effective deposition of calaverite and hessite requires a regime of decreasing $aHS^-_{(aq)}$ and increasing $aHTe^-_{(aq)}$ or at the very least decreasing $aHS^-_{(aq)}$ at constant $aHTe^-_{(aq)}$ or increasing $aHTe^-_{(aq)}$ at constant $aHS^-_{(aq)}$. Boiling, however, decreases the activity of both HS^- and HTe^- in the liquid by preferentially fractionating them into the vapor. Moreover, as shown by McPhail (1995) and Grundler et al. (2013) H_2Te

Zhai, D. G., A. E. Williams-Jones, J. J. Liu, S. F. Tombros, and N. J. Cook.
"Mineralogical, Fluid Inclusion, and Multiple Isotope (H-O-S-Pb) Constraints on the Genesis of the Sandaowanzi Epithermal Au-Ag-Te Deposit, Ne China."
Economic Geology 113, no. 6 (Sep 2018): 1359-82. http://dx.doi.org/10.5382/econgeo.2018.4595.

partitions particularly strongly into the vapor (perhaps even more strongly than H_2S). Thus, in the context of these parameters, boiling will not promote telluride deposition. Another effect of boiling is to sharply decrease temperature. As shown, in Figure 17, this effect of boiling, instead of promoting telluride deposition, will actually promote its dissolution. The other effects of boiling, increasing the pH of the fluid and lowering fH_2, also do not provide a satisfactory explanation for the observed deposition of hessite and calaverite, because, whereas decreasing pH promotes deposition of hessite, this is not true for calaverite and decreasing fH_2 only promotes deposition of calaverite. Thus, in summary, it is very unlikely that the Sandaowanzi gold-telluride formed as a result of boiling, despite the extensive evidence for this phenomenon

The widespread pyritization of the host rock particularly in the immediate vicinity of the gold-telluride quartz veins suggest that sulfidation was temporally associated with ore formation. Sulfidation would have significantly decreased the activity of $HS^-_{(aq)}$ in the ore fluids, driving Reactions 6 and 7 to the right thereby promoting precipitation of hessite and calaverite (this is also illustrated in Figure 17). We therefore propose that sulfidation played a significant role in Au-Ag telluride deposition.

A more important control on Au-Ag telluride deposition is suggested by the behaviour of Te in hydrothermal fluids. Whereas tellurium solubilitiy is extremely low in auriferous liquids, e.g., 0.005 to 5 ppb at 300°C (McPhail 1995), it can reach ppm concentrations in vapors at the same temperature (Grundler et al. 2013). This provides compelling evidence that the tellurium was not transported with the gold. We therefore propose, as have Cooke and McPhail (2001), that tellurium was introduced into the dominantly meteoric auriferous fluid at the site of ore deposition by a magmatic vapor derived from the coeval trachyandesite magma, which condensed on contact with the ore fluid. This instantly increased $a\mathrm{HTe}^-_{(aq)}$, driving Reactions 6 and 7 to the right, thereby causing massive gold- and silver-telluride precipitation. Evidence of the potential importance of this process, particularly for gold, is illustrated by Figure 17, in which it can be seen that less that a log unit increase in $a\mathrm{HTe}^-_{(aq)}$ will lead to deposition of 99% of the dissolved gold and a four log unit increase in $a\mathrm{HTe}^-_{(aq)}$ will lead to deposition of 99% the silver.

In summary, we propose that condensation of H_2Te vapor into the ore fluid was the principal control of ore deposition and that sulfidation played a subordinate role by lowering the activity of

Zhai, D. G., A. E. Williams-Jones, J. J. Liu, S. F. Tombros, and N. J. Cook.
"Mineralogical, Fluid Inclusion, and Multiple Isotope (H-O-S-Pb) Constraints on the Genesis of the Sandaowanzi Epithermal Au-Ag-Te Deposit, Ne China."
Economic Geology 113, no. 6 (Sep 2018): 1359-82. http://dx.doi.org/10.5382/econgeo.2018.4595.

HS- thereby destabilizing the bisulphide species that were responsible for silver and gold transport. We further propose that condensation of the H_2Te vapor and sulfidation were considerably more efficient in depositing gold (Fig. 17a) than silver (Fig. 17b), which may help explain why much more gold-bearing telluride than silver-bearing telluride formed in the deposit.

The end of Stage III was marked by deposition of Cu-Zn and Pb-Zn-Cu alloys, implying that neither tellurium nor sulfur was available to act as depositional ligands as almost all the $HS^-_{(aq)}$ and $HTe^-_{(aq)}$ had been consumed in earlier reactions. The model of telluride-dominant ore formation proposed above for the Sandaowanzi deposit, is also likely other large epithermal Au-Ag-Te deposits (e.g., Emperor, Fiji; Porgera, Papua New Guinea; Acupan, Philippines; Cripple Creek, Colorado).

Conclusions

The low-sulfidation Sandaowanzi Au-Ag-Te deposit in NE China is unusual because the bulk of the gold is present as coarse-grained tellurides within bonanza Au ores (up to 35,000 g/t). Fluid inclusion microthermometric data show that the gold-silver telluride ores deposited from an epithermal system emplaced at a depth of < 1 km that boiled intensely and cooled from a temperature in excess of 300 °C to a temperature less than 200 °C at a pressure that approached hydrostatic. The $\delta^{18}O_{H2O}$ and δD_{H2O} isotopic values and importance of Ca^{2+} and sulfur species in the fluid are consistent with a meteoric water-dominant hydrothermal system that underwent significant interaction with its host rocks. In contrast, the $\delta^{34}S_{H2S}$ isotopic composition of the fluids and the lead isotope ratios of the sulfides are indicative of a magmatic source for the sulfur and metals, which is interpreted to indicate that sulfur and metals were leached from the host trachyandesites. Although fluid boiling is commonly invoked to explain the genesis of adularia-sericite (low sulfidation) epithermal deposits, this mechanism cannot explain the genesis of the Sandaowanzi Au-Ag-Te deposit. Instead, we show that the deposit owes its origin to a H_2Te vapor, which was derived from the coeval alkaline magma and condensed in the dominantly meteoric ore fluid; sulfidation of the host rocks contributed to the deposition by destabilizing the gold and silver bisulfide species. This study emphasizes the importance of fluid-rock interaction and the mixing of low density magmatic fluids with meteoric waters in producing World class Au- and Ag-telluride

Zhai, D. G., A. E. Williams-Jones, J. J. Liu, S. F. Tombros, and N. J. Cook.
"Mineralogical, Fluid Inclusion, and Multiple Isotope (H-O-S-Pb) Constraints on the Genesis of the Sandaowanzi Epithermal Au-Ag-Te Deposit, Ne China."
Economic Geology 113, no. 6 (Sep 2018): 1359-82. http://dx.doi.org/10.5382/econgeo.2018.4595.

deposits.

Acknowledgements

This research was supported by the National Natural Science Foundation of China (Grants 41573036, 40973035). We thank Rich Goldfarb, Karen Kelley, Edward Ripley and David Cooke for reading an early version of the manuscript and making helpful suggestions. We greatly appreciate Dr. Richen Zhong for making available his Unitherm database, which enabled some of the thermodynamic modeling. We acknowledge the constructive reviews of Drs. Noel White and Hong-Rui Fan that helped improve this paper, and associate editor Huayong Chen and Editor in Chief Georges Beaudoin for their editorial help. Revision of this manuscript was completed during DZ's visit to McGill University. Travel and living expenses in Canada were financially supported by an international visiting program grant from the Fundamental Research Funds for the Central Universities China.

References

Afifi AM, Kelly WC, Essene EJ (1988) Phase relations among tellurides, sulfides, and oxides: I. Thermochemical data and calculated equilibria. Econ Geol 83: 377-294

Ahmad M, Solomon M, Washe JL (1987) Mineralogical and geochemical studies of the Emperor gold telluride deposit, Fiji. Econ Geol 82: 345-370

Bodnar RJ, Sanchez PL, Moncada D, Steele-MacInnes M (2014) Fluid inclusions in hydrothermal ore deposits. Treatise on Geochem 13: 119-142

Brown PE (1989) FLINCOR: A microcomputer program for the reduction and investigation of fluid inclusion data. Am Mineral 74: 1390-1393

Brown PE, Lamb WE (1989) P-V-T properties of fluids in the system NaCl ± H_2O ± CO_2: New graphical presentations and implications for fluid inclusions studies. Geochim Cosmochim Acta 53: 1209-1221

Chen J, Sun FY (2011) Zircon U-Pb ages of Sandaowanzi gold deposit and its geological significance, Heilongjiang province. Gold 5: 18–22 (in Chinese with English abstract)

Chen J, Sun FY, He SY, Huo L, Shu SL, Ren H, Zhang QM (2012) Analysis on fluid inclusion characteristics and genesis of Sandaowanzi gold deposit in Heilongjiang. Gold 1: 8–14 (in Chinese with English abstract)

581 Cheng L, Peng XL, Han JL, Ren L, Liu Y (2017) Geochronology, geochemistry, and geological implications of
582 volcanic-subvolcanic rocks of Sandaowanzi gold deposit in Heilongjiang Province, NE China. Global Geol 36:
583 460-673 (in Chinese with English abstract)
584 Ciobanu CL, Cook NJ, Pring A, Damian G (2008) Another look at nagyágite from the type locality, Săcărîmb,
585 Romania: Replacement, chemical variation and petrogenetic implications. Miner Petrol 93: 273-307
586 Ciobanu CL, Cook NJ, Spry PG (2006) Preface–Special Issue: Telluride and selenide minerals in gold deposits–how
587 and why?. Miner Petrol *87*: 163-169
588 Clayton RN, Mayeda TK (1963) The use of bromine pentafluoride in the extraction of oxygen from oxides and silicates
589 for isotopic analysis. Geochim Cosmochim Acta 27: 43-52
590 Coleman ML, Sheppard TJ, Durham JJ, Rouse JE, Moore GR (1982) Reduction of water with zinc for hydrogen isotope
591 analysis. Anal Chem 54: 993–995
592 Cooke DR, McPhail DC (2001) Epithermal Au-Ag-Te mineralization, Acupan, Baguio district, Philippines: numerical
593 simulations of mineral deposition. Econ Geol 96: 109-131
594 Fan WM, Guo F, Wang YJ, Lin G (2003) Late Mesozoic calc-alkaline volcanism of post-orogenic extension in the
595 northern Da Hinggan Mountains, Northeastern China. J Volcano Geotherm Res 121: 115–135
596 Fritz P, Drimmie RJ, Norwick K (1974) Preparation of sulfur dioxide for mass spectrometer analysis by combustion of
597 sulfide with copper oxide. Anal Chem 76: 164-166
598 Gao S, Xu H, Zang Y, Yang L, Yang B, Wang T (2017) Late Mesozoic magmatism and metallogeny in NE China: The
599 Sandaowanzi–Beidagou example. Int Geol Rev 59: 1413-1438
600 Giggenbach WF (1992) Isotopic shifts in waters from geothermal and volcanic systems along convergent plate
601 boundaries and their origin. Earth Planet Sci Lett 113: 495-510
602 Goldfarb RJ, Taylor RD, Collins GS, Goryachev NA, Orlandini OF (2014) Phanerozoic continental growth and gold
603 metallogeny of Asia. Gondwana Res 25(1): 48-102
604 Goldstein RH, Reynolds TJ (1994) Systematics of fluid inclusions in diagenetic minerals. Society of Sedimentary
605 Geology (SEPM) Short Course 31: 199
606 Grootenboer J, Schwarcz HP (1969) Experimentally determined sulfur isotope fractionations between sulfide minerals.
607 Earth Planet Sci Lett 7: 162-166
608 Grundler PV, Brugger J, Etschmann BE, Helm L, Liu W, Spry PG, Tian Y, Testemale D, Pring A (2013) Speciation of
609 aqueous tellurium (IV) in hydrothermal solutions and vapors, and the role of oxidized tellurium species in Te
610 transport and gold deposition. Geochim Cosmochim Acta 120: 298-325

Zhai, D. G., A. E. Williams-Jones, J. J. Liu, S. F. Tombros, and N. J. Cook.
"Mineralogical, Fluid Inclusion, and Multiple Isotope (H-O-S-Pb) Constraints on the Genesis of the Sandaowanzi Epithermal Au-Ag-Te Deposit, Ne China."
Economic Geology 113, no. 6 (Sep 2018): 1359-82. http://dx.doi.org/10.5382/econgeo.2018.4595.

611 Han SY, Zhai DG, Liu JJ, Lu J, Wu SH, Yang LB (2011) Mineral assemblage of Sandaowanzi tellurium-gold deposit in
612 Heilongjiang province and its genetic significance. Miner Deposits 30: 855-66 (in Chinese with English abstract)
613 Hedenquist JW, Lowenstern JB (1994) The role of magmas in the formation of hydrothermal ore deposits. Nature 370:
614 519-527
615 Hoefs J (2009) Stable Isotope Geochemistry. Berlin, Springer-Verlag, 285
616 Hu HB, Mao JW, Niu SY, Li YF, Li MW (2006) Geology and geochemistry of telluride-bearing Au deposits in the
617 Pingyi area, Western Shandong, China. Miner Petrol 87: 209-240
618 Jensen EP, Barton MD (2000) Gold deposits related to alkaline magmatism. In: Hagemann SG, Brown PE (eds) Gold in
619 2000, *Rev Econ Geol 13*: 279-314
620 Johnson JW, Oelkers EH, Helgeson HC (1992) SUPCRT92: A software package for calculating the standard molal
621 thermodynamic properties of minerals, gases, aqueous species and reactions from 1 to 5000 bars and 0° to 1000°C.
622 Comput Geosci 18: 899-947
623 Kelley KD, Romberger SB, Beaty DW, Pontius JA, Snee LW, Stein HJ, Thompson TB (1998) Geochemical and
624 geochronological constraints on the genesis of Au-Te deposits at Cripple Creek, Colorado. Econ Geol 93:
625 981-1012
626 Kong HQ, Wang JM, Zhang SQ, Sun L (2006) Geophysical analyses of Heihe Sandaowanzi gold deposit, Heilongjiang
627 Province. Gold 27: 10-13 (in Chinese with English abstract)
628 Kovalenker VA, Safonov YG, Naumov VB, Rusinov VL (1997) The epithermal gold-telluride Kochbulak deposit
629 (Uzbekistan). Geol Ore Deposits 39: 107-128
630 Liu BS, Lu J (2006) Geological, geochemical and genetic study of the Sandaowanzi quartz vein type gold deposit in
631 Heihe city, Heilongjiang province. Geotectonica et Metallogenia 30: 481-485 (in Chinese with English abstract)
632 Liu J, Zhai D, Dai H, de Fourestier J, Yu C, Gu X, Wang Y, Yu H, Wang J, Liu Z (2017) Nanoscale characterization of
633 Au_2Te grains from the Sandaowanzi gold deposit, northeast China. Can Mineral 55: 181-194
634 Liu JL, Bai XD, Zhao SJ, Tran M, Zhang ZC, Zhao ZD, Zhao HB, Lu J (2011) Geology of the Sandaowanzi telluride
635 gold deposit of the northern Great Xing'an Range, NE China: Geochronology and tectonic controls. J Asian Earth
636 Sci 41: 107–118
637 Liu JL, Zhao SJ, Cook NJ, Bai XD, Zhang, ZC, Zhao ZD, Zhao HB, Lu J (2013) Bonanza-grade accumulations of gold
638 tellurides in the Early Cretaceous Sandaowanzi deposit, northeast China. Ore Geol Rev 54: 110-126
639 Lu J, Liu XG, Han ZZ, Zhang AK, Zhao HD, Li DR (2009b) A study on ore features and gold occurrence state of the
640 Sandaowanzi gold deposit. Geol Explor 45: 395-401 (in Chinese with English abstract)
641 Lu J, Wang JM, Yue BJ, Wang HB, Yu RW, Zhao LG (2005) Fluid inclusion and stable isotope geochemistry of

Zhai, D. G., A. E. Williams-Jones, J. J. Liu, S. F. Tombros, and N. J. Cook.
"Mineralogical, Fluid Inclusion, and Multiple Isotope (H-O-S-Pb) Constraints on the Genesis of the Sandaowanzi Epithermal Au-Ag-Te Deposit, Ne China."
Economic Geology 113, no. 6 (Sep 2018): 1359-82. http://dx.doi.org/10.5382/econgeo.2018.4595.

642 Sandaowanzi gold deposit. Geol Prospecting 41: 33–37 (in Chinese with English abstract)
643 Lu J, Zhao ZD, Cao YP, Han ZZ, Zhang AQ, Yu JC (2009a) Geological characteristics and genesis of the Sandaowanzi
644 gold deposit in Heilongjiang Province. Geol China 36: 853–860 (in Chinese with English abstract)
645 Mao JW, Chen YC, Wang PA (1995) Geology and geochemistry of the Dashuigou tellurium deposit, western Sichuan,
646 China. Int Geol Rev 37: 526-546
647 Mao JW, Pirajno F, Cook N (2011) Mesozoic metallogeny in East China corresponding geodynamic settings — An
648 introduction to the special issue. Ore Geol Rev 43: 1-7
649 Mao JW, Wang YT, Zhang ZH, Yu JJ, Niu BG (2003) Geodynamic settings of Mesozoic large-scale mineralization in
650 North China and adjacent areas. Sci China D 46: 838-851
651 McPhail DC (1995) Thermodynamic properties of aqueous tellurium species between 25°C and 250°C. Geochim
652 Cosmochim Acta 59: 851-866
653 Niu SY, Guo LJ, Liu JM, Shao JA, Wang BD, Hu HB, Sun AQ, Wang S (2006) Tectonic ore-controlling in the
654 middle-southern segment of Da Hinggan Ling, Northeast China. Chin J Geochem 25: 62-70.
655 Ohmoto H, Lasaga AC (1982) Kinetics of reactions between aqueous sulfates and sulfides in hydrothermal systems.
656 Geochim Cosmochim Acta 46: 1727–1745
657 Ohmoto H, Rye RO (1979) Isotopes of sulfur and carbon, in Barnes, HL, ed, Geochemistry of hydrothermal ore
658 deposits: New York, Wiley Interscience, p 509–567
659 Pals DW, Spry PG (2003) Telluride mineralogy of the low-sulfidation epithermal Emperor gold deposit, Vatukoula,
660 Fiji. Miner Petrol 79: 285–307
661 Pirajno F (2013) Large igneous provinces (Xiong'er, Dashigou, 827 Ma Event, Tarim, Emeishan) and the Yanshanian
662 tectono-thermal Event event of Eastern China. The Geology and Tectonic Settings of China's Mineral Deposits,
663 Springer, Netherlands, 671 p
664 Porter EW, Ripley EM (1985) Petrologic and stable isotope study of the gold-bearing breccia pipe at the Golden
665 Sunlight deposit, Montana. Econ Geol 80: 1689-1706
666 Qi JP, Chen YJ, Pirajno F (2005) Geological characteristics and tectonic setting of the epithermal deposits in the
667 northeast China. J Min Petro Sci 25: 47–59 (in Chinese with English abstract)
668 Richards JP (1990) Petrology and geochemistry of alkalic intrusives at the Porgera gold deposit, Papua New Guinea. J
669 Geochem Explor 35: 141-199
670 Richards JP, Kerrich R (1993) The Porgera gold mine, Papua New Guinea: Magmatic, hydrothermal to epithermal
671 evolution of an alkalic-type precious metal deposit. Econ Geol 88: 755-781
672 Salvi S, Williams-Jones AE (1997) Fluid-inclusion volatile analysis by gas chromatography: application of a wide-bore
673 porous-polymer capillary column to the separation of organic and inorganic compounds. Can Mineral *35*:
674 1391-1414.
675 Saunders JA (1991) Gold deposits of the Boulder County gold district, Colorado. U.S. Geological Survey Bulletin
676 1857-I: 137-148

Shelton KL, So CS., Haeussler GT, Chi SJ, Lee KY (1990) Geochemical studies of the Tongyoung gold-silver deposits, Republic of Korea: evidence of meteoric water dominance in a Te-bearing epithermal system. Econ Geol 85: 1114-1132

Shvarov Y (2011) Unitherm Software, version 4.4

Sillitoe RH (2002) Some metallogenic features of gold and copper deposits related to alkaline rocks and consequences for exploration. Mineral Deposita *37*: 4-13

Simmons SF, White NC, John DA (2005) Geological characteristics of epithermal precious and base metal deposits: Econ Geol 100th Anniversary Volume: 485-522

Simon AC, Frank MR, Pettke T, Candela PA, Piccoli PM, Heinrich CA (2005) Gold partitioning in melt-vapor-brine systems. Geochim Cosmochim Acta 69: 3321-3335

Simon G, Essene EJ (1996) Phase relations among selenides, sulfides, tellurides, and oxides: I. Thermodynamic properties and calculated equilibria. Econ Geol 91: 1183-1208

Spry PG, Foster F, Truckle JS, Chadwick TH (1997) The mineralogy of the Golden Sunlight gold-silver telluride deposit, Whitehall, Montana, USA. Miner Petrol 59: 143–164

Steele-MacInnis M, Lecumberri-Sanchez P, Bodnar RJ (2012) HOKIEFLINCS_H2O-NACL: A Microsoft Excel spreadsheet for interpreting microthermometric data from fluid inclusions based on the PVTX properties of H_2O–NaCl. Comput Geosci 49: 334-337

Thompson TB, Trippel AD, Dwelley PC (1985) Mineralized veins and breccias of the Cripple Creek district, Colorado. Econ Geol 80: 1669-1688

Tombros SF, Seymour KS, Williams-Jones AE (2010) Controls on tellurium in base, precious, and telluride minerals in the Panormos Bay Ag-Au-Te deposits, Tinos Island, Cyclades, Greece. Econ Geol 105: 1097–1111

Tombros SF, Seymour KS, Williams-Jones AE, Spry PG (2008) Later stages of evolution of an epithermal system: Au-Ag mineralizations at Apigania Bay, Tinos Island, Cyclades, Hellas, Greece. Miner Petrol 94: 175-194

Tran M, Liu JL, Hu JJ, Zou YX, Zhang HY (2008) Discovery and geological significance of Sandaowanzi telluride type gold deposit in the northern Daxing′anling, Heilongjiang, China. Geol Bull China 27: 548–587 (in Chinese with English abstract)

Wang F, Zhou XH, Zhang LC, Ying JF, Zhang YT, Wu FY, Zhu RX (2006) Late Mesozoic volcanism in the Great Xing'an Range (NE China): Timing and implications for the dynamic setting of NE Asia. *Earth Planet Sci Lett* 251: 179–198

Wang SS, Liu JY, Ji HW, Lv J, Zhou S, Liu JL (2017) Geochronology and geochemistry of the andesites of Longjiang Formation in the Sandaowanzi gold deposit, Heilongjiang Province. Acta Petrol Sin 33(8): 2604-2618 (in Chinese with English abstract)

Wilde SA (2015) Final amalgamation of the Central Asian Orogenic Belt in NE China: Paleo-Asian Ocean closure versus Paleo-Pacific plate subduction—A review of the evidence. Tectonophysics 662: 345-362

Williams-Jones AE, Heinrich CA (2005) Vapor transport of metals and the formation of magmatic-hydrothermal ore deposits. Econ Geol 100: 1287-1312

Wu FY, Sun DY, Li HM, Jahn BM, Wilde SA (2002) A–type granites in Northeastern China: Age and geochemical constraints on their petrogenesis. Chem Geol 187: 143–173

Zhai, D. G., A. E. Williams-Jones, J. J. Liu, S. F. Tombros, and N. J. Cook.
"Mineralogical, Fluid Inclusion, and Multiple Isotope (H-O-S-Pb) Constraints on the Genesis of the Sandaowanzi Epithermal Au-Ag-Te Deposit, Ne China."
Economic Geology 113, no. 6 (Sep 2018): 1359-82. http://dx.doi.org/10.5382/econgeo.2018.4595.

Wu FY, Yang JH, Wilde SA, Zhang XO (2005) Geochronology, petrogenesis and tectonic implications of Jurassic granites in the Liaodong Peninsula, NE China. Chem Geol 221: 127–156

Wu HY, Zhang LC, Wan B, Chen ZG, Xiang P, Pirajno F, Du AD, Qu WJ (2011) Re–Os $^{40}Ar/^{39}Ar$ ages of the Jiguanshan porphyry Mo deposit, Xilamulun metallogenic belt, NE China, constraints on mineralization events. Mineral Deposita 46: 171–185

Wu ZY, Wang HB, Xu DH, Zhou YC (2005) Geological and geochemical studies of the Sandaowanzi gold deposit, Heihe County, Helongjiang Province. Geol Rev 51: 264–-267 (in Chinese with English abstract)

Xu H, Yu Y, Wu X, Yang L, Tian Z, Gao S, Wang Q (2012) Intergrowth texture in Au-Ag-Te minerals from Sandaowanzi gold deposit, Heilongjiang Province: Implications for ore-forming environment. Chin Sci Bull 57: 2778-2786

Xu H, Yu YX, Gao S, Tian Z, Wu XK, Yang LJ, Wang QS, Sun Y (2011) A new crystalline compound of Au-Te in Sandaowanzi gold deposit, Heilongjiang Province. Geol Bull China 30: 1779-1784 (in Chinese with English abstract)

Yu YX, Xu H, Wu XK, Yang LJ, Tian Z, Gao S, Wang QS (2012) Characteristics of the Au-Ag-Te minerals and its ore-forming fluids in Sandaowanzi gold deposit, Heilongjiang Province. Acta Petrol Sin 28: 345–356 (in Chinese with English abstract)

Zartman RE, Doe BR (1981) Plumbotectonics—the model. Tectonophysics 75: 135-162

Zhai D, Liu J (2014) Gold-telluride-sulfide association in the Sandaowanzi epithermal Au-Ag-Te deposit, NE China: implications for phase equilibrium and physicochemical conditions. Miner Petrol 108, 853-871

Zhai D, Liu J, Ripley EM, Wang J (2015) Geochronological and He–Ar–S isotopic constraints on the origin of the Sandaowanzi gold-telluride deposit, northeastern China. Lithos 212, 338-352

Zhai D, Liu J, Tombros S, Williams-Jones AE (2017a) The genesis of the Hashitu porphyry molybdenum deposit, Inner Mongolia, NE China: constraints from mineralogical, fluid inclusion, and multiple isotope (H, O, S, Mo, Pb) studies. Miner Deposita: DOI: 10.1007/s00126-017-0745-5

Zhai D, Liu J, Zhang A, Sun Y (2017b) U-Pb, Re-Os and $^{40}Ar/^{39}Ar$ geochronology of porphyry Sn ± Cu ± Mo and polymetallic (Ag-Pb-Zn-Cu) vein mineralization at Bianjiadayuan, Inner Mongolia, NE China: Implications for discrete mineralization events. Econ Geol 112: 2041-2059

Zhai DG, Liu JJ, Han SY, Wang JP, Zhang HY, Liu ZJ, Yang LB, Zhang HF, Lu J (2013) Typomorphic characteristics of pyrite and processes of changes and preservation of the Sandaowanzi telluride-gold deposit in Heilongjiang province. Acta Geol Sin 87: 81-90 (in Chinese with English abstract)

Zhai DG, Liu JJ, Wang JP, Yang YQ, Zhang HY, Wang XL, Zhang QB, Wang GW, Liu ZJ (2014) Zircon U–Pb and molybdenite Re–Os geochronology, and whole–rock geochemistry of the Hashitu molybdenum deposit and host granitoids, Inner Mongolia, NE China. J Asian Earth Sci 79: 144–160

Zhang JH, Ge WC, Wu FY, Wilde SA, Yang JH, Liu XM (2008) Large-scale Early Cretaceous volcanic events in the northern Great Xing'an Range, northeastern China. Lithos 102: 138-157

Zhang XM, Spry PG (1994) Petrological, mineralogical, fluid Inclusion, and stable isotope studies of the Gies gold-silver telluride deposit, Judith Mountains, Montana. Econ Geol 89: 602-627

Zhao SJ, Liu JL, Bai XD, Zhao HB, Lu J, Chen Y, Tran M (2010) Fluid inclusions and sulfur isotopes of Sandaowanzi gold telluride deposit, Heilongjiang Province. Miner Deposits 29: 476-488 (in Chinese with English abstract)

Zhai, D. G., A. E. Williams-Jones, J. J. Liu, S. F. Tombros, and N. J. Cook.
"Mineralogical, Fluid Inclusion, and Multiple Isotope (H-O-S-Pb) Constraints on the Genesis of the Sandaowanzi Epithermal Au-Ag-Te Deposit, Ne China."
Economic Geology 113, no. 6 (Sep 2018): 1359-82. http://dx.doi.org/10.5382/econgeo.2018.4595.

Zhao TY, Zhao HB, Sun FY, Liu JL (2013) Metallogenic epoch of the Sandaowanzi gold deposit in Heilongjiang Province: constraints from the evidence of isotopic age. Geol China 40: 1202-1208 (in Chinese with English abstract)

Zheng YF (1993) Calculation of oxygen isotope fractionation in anhydrous silicate minerals. Geochim Cosmochim Acta 57: 1079-1091

Zimmer K, Zhang Y, Lu P, Chen Y, Zhang G, Dalkilic M, Zhu C (2016) SUPCRTBL: A revised and extended thermodynamic dataset and software package of SUPCRT92. Comput Geosci 90: 97-111

Figure Captions

Fig. 1. (a): Map showing the location of the Sandaowanzi deposit in relation to the tectonic framework in the Great Hinggan Range Metallogenic Belt, northeastern China, and the distribution of Mesozoic volcanic rocks in eastern China (based on Wu et al. 2005). Abbreviations: NCC–North China Craton, YC–Yangtze Craton, SECOB–South East China Orogenic Belt; (b): Generalized geological map of the Great Hinggan Range (modified after Qi et al. 2005), (c): Map showing general geology of the Sandaowanzi area (modified after Lu et al. 2005).

Fig. 2. Detailed geological map of the Sandaowanzi gold-telluride deposit (modified after Lu et al. 2005).

Fig. 3. Geological cross section of the Sandaowanzi veins and gold-telluride orebody (modified after Lu et al. 2005).

Fig. 4. Photographs showing Sandaowanzi quartz veins: (a). Sandaowanzi ore-bearing quartz veins hosted in trachyandesite; (b). Mineralized quartz veins were oxidized in outcrops in which the trachyandesite was intensively altered and brecciated; (c). Banded milky, grey and clear quartz veins; milky quartz shows colloform banding (enlarged square in dashed lines); stage II sulfide-telluride and stage III telluride mineralization are associated with grey quartz and clear quartz veins, respectively; (d). Banded milky, grey, clear and white quartz veins; milky quartz shows comb and vuggy textures; stage II sulfide-telluride and stage III telluride and native gold mineralization (enlarged square in dashed lines) are associated with grey quartz and clear quartz veins, respectively; (e). Banded milky, grey (with sulfide and telluride mineralization) and clear quartz (with telluride mineralization) veins; milky quartz may occur as breccias in grey quartz (associated with sulfide and telluride mineralization); clear quartz contains telluride mineralization; (f). Complex relationships between different quartz veins showing milky quartz contains abundant angular fragments of altered trachyandesite, and pyrite grains, and is commonly replaced by grey quartz, whereas

Zhai, D. G., A. E. Williams-Jones, J. J. Liu, S. F. Tombros, and N. J. Cook.
"Mineralogical, Fluid Inclusion, and Multiple Isotope (H-O-S-Pb) Constraints on the Genesis of the Sandaowanzi Epithermal Au-Ag-Te Deposit, Ne China."
Economic Geology 113, no. 6 (Sep 2018): 1359-82. http://dx.doi.org/10.5382/econgeo.2018.4595.

782 milky, grey and white quartz veins are occasionally intruded by clear quartz veins, mostly reflecting multiple
783 episodes of quartz precipitation. Scale bar on c-f is 1 cm.
784 Abbreviations: CQ–clear quartz, GQ–grey quartz, MQ–milky quartz, Au–native gold, Py–pyrite,
785 S-Te–sulfide-telluride, Te–telluride, T–trachyandesites, WQ–white quartz.
786 Fig. 5. Photomicrographs of representative sulfide and telluride mineralization at Sandaowanzi. (a):
787 Intergrowth of petzite-calaverite with galena and sphalerite in stage II grey quartz veins (BSE), (b): Altaite
788 coexisting with petzite from clear quartz veins in stage III (BSE), (c): Hessite and petzite intergrowth with
789 anilite in stage III clear quartz veins (BSE), (d): Intergrowth of altaite, petzite, hessite and chalcopyrite in
790 stage III, and stage IV native gold with crack-filling textures (reflected light), (e):
791 Sylvanite-krennerite-calaverite assemblage replacing petzite-hessite assemblage and is intergrown with or
792 replaced by native gold and chalcopyrite, and these assemblages occur in stage III clear quartz (reflected
793 light), (f): Stage III sylvanite intergrown with chalcopyrite and replacing stage II sphalerite, which is
794 replaced by tennantite (reflected light), (g): Stage III petzite and calaverite, which are associated with an
795 assemblage calaverite-gold at nano-scale (BSE), (h): Stage III sylvanite containing inclusions of altaite and
796 stage II sphalerite, and all three minerals are replaced by stage III tetrahedrite (BSE), (i): Stage III
797 petzite-hessite assemblage replaces stage II chalcopyrite and sphalerite (BSE).
798 Abbreviations: Alt-altaite, Ani-anilite, Au-native gold, Cav-calaverite, Cp-chalcopyrite, Gn-galena,
799 Hes-hessite, Kre-krennerite, Ptz-petzite, Qtz-quartz, Sp-sphalerite, Syl-sylvanite, Td-tetrahedrite,
800 Tn-tennantite.
801 Fig. 6. SEM-CL textures in Sandaowanzi hydrothermal quartz. (a) Obvious oscillatory euhedral growth
802 zones observed in hydrothermal vein quartz; (b) Quartz with oscillatory euhedral growth zones replaced by
803 late stage quartz with growth zones; (c)-(d) Hydrothermal vein quartz grains with oscillatory euhedral
804 growth zones destroyed and surrounded by late stage quartz; (e)-(f) Quartz with euhedral growth zones cut
805 by fractures and replaced by late relatively homogenous quartz.
806 Fig. 7. Photomicrographs of fluid inclusion assemblages in Sandaowanzi quartz veins. (a) and (b): Primary
807 L-V type inclusions occur in growth zones, whereas the secondary inclusions are arranged in parallel trails
808 that are aligned along fractures and terminate at crystal growth surfaces. Figure (b) is an enlargement of the
809 black square in (a), (c): Fluid inclusion assemblages with variable vapor-liquid ratios, (d): Coexisting of
810 primary L-V and V-L type inclusions in one growth zone, (e): Primary L-V and L-V-S type inclusions, and (f

Zhai, D. G., A. E. Williams-Jones, J. J. Liu, S. F. Tombros, and N. J. Cook.
"Mineralogical, Fluid Inclusion, and Multiple Isotope (H-O-S-Pb) Constraints on the Genesis of the Sandaowanzi Epithermal Au-Ag-Te Deposit, Ne China."
Economic Geology 113, no. 6 (Sep 2018): 1359-82. http://dx.doi.org/10.5382/econgeo.2018.4595.

and g): Primary L-V-S and L-V inclusions (vapor bubble occupies up to ≈ 35 vol. %). Photographed at + 25°C in plane-polarized, transmitted light (L_{H2O}= aqueous liquid, V_{H2O} = vapor).

Fig. 8. Histograms of homogenization temperature and salinity of fluid inclusions from different stage quartz veins in the Sandaowanzi deposit.

Fig. 9. Homogenization temperature versus salinity plots in the NaCl-H_2O system for different stage fluid inclusion assemblages from the Sandaowanzi deposit. Vertical line represents the boiling FIA.

Fig. 10. Histogram of $\delta^{34}S_{H2S}$ isotopic compositions of the Sandaowanzi ore fluids in isotopic equilibrium with pyrite and chalcopyrite. Most of the data are from Lu et al. (2005), Liu and Lu (2006) and Zhao et al. (2010).

Fig. 11 $^{206}Pb/^{204}Pb$ versus $^{207}Pb/^{204}Pb$ uranogenic (a) and $^{206}Pb/^{204}Pb$ versus $^{208}Pb/^{204}Pb$ thorogenic (b) plots of pyrite and whole-rock samples (based on Zartman and Doe 1981).

Fig. 12. $\delta^{18}O$ versus δD diagram showing mineralizing fluid compositions at Sandaowanzi. Fields of volcanic vapors, felsic magmas and magmatic water are based on Hedenquist and Lowenstern (1994). The metamorphic water boxes and the kaolinite weathering and meteoric water lines are adopted from Giggenbach (1992) and Hoefs (2009). D-O isotope patterns of Qtz-Cal-Ad±Sec±Illite and Qtz-Alun±Dick±Kao type epithermal deposits are based on Simmons et al. (2005). Some data are collected from Lu et al. (2009).

Fig. 13. Variations of $\delta^{18}O_{H2O}$, δD_{H2O}, and $\delta^{34}S_{H2S}$ isotopic compositions of hydrothermal fluids with depth from the Sandaowanzi deposit.

Fig. 14. Activity-activity diagrams showing Sandaowanzi mineralizing fluids in equilibrium with alteration minerals at different temperatures. (a): $Log(\alpha_{K^+}/\alpha_{H^+})$ versus $log(\alpha_{Na^+}/\alpha_{H^+})$ in the K_2O-Na_2O-Al_2O_3-SiO_2-H_2O system; (b): $Log(\alpha_{K^+}/\alpha_{H^+})$ versus $log[\alpha_{Ca^{++}}/(\alpha_{H^+})^2]$ in the K_2O-CaO-Al_2O_3-SiO_2-H_2O system; (c): $Log(\alpha_{K^+}/\alpha_{H^+})$ versus $log[\alpha_{Mg^{++}}/(\alpha_{H^+})^2]$ in the K_2O-MgO-Al_2O_3-SiO_2-H_2O system; (d): $Log[\alpha_{Mg^{++}}/(\alpha_{H^+})^2]$ versus $log[\alpha_{Ca^{++}}/(\alpha_{H^+})^2]$ in the CaO-MgO-Al_2O_3-SiO_2-H_2O system. The blue, pink and green squares represent the equilibrium for stages I, II and III, respectively, and the thermodynamic data were derived from SUPCRT92 database (Johnson 1992).

Fig. 15. LogfO_2 versus pH diagrams showing stability relationships in the Fe-Cu-O-S system. (a): For stage I, at 330°C and 180 bars. Dotted lines represent the field boundaries of the principal aqueous sulfur species and thicker dashed lines represent the stability field boundaries for pyrite, pyrrhotite, hematite and magnetite.

Zhai, D. G., A. E. Williams-Jones, J. J. Liu, S. F. Tombros, and N. J. Cook.
"Mineralogical, Fluid Inclusion, and Multiple Isotope (H-O-S-Pb) Constraints on the Genesis of the Sandaowanzi Epithermal Au-Ag-Te Deposit, Ne China."
Economic Geology 113, no. 6 (Sep 2018): 1359-82. http://dx.doi.org/10.5382/econgeo.2018.4595.

840 The stability boundary for the orthoclase-illite equilibrium is also shown, and the square represents
841 constrained physicochemical conditions for stage I mineralization, (b): For stage II, at 280°C and 120 bars.
842 Solid thick line is the stability field boundary for the equilibrium bornite + pyrite = chalcopyrite, at 280°C.
843 Dotted lines represent the field boundaries of the principal aqueous sulfur and tellurium species. Thicker
844 dashed and dashed-dotted lines represent the stability field boundaries for Fe-O-S minerals and anglesite and
845 galena, respectively. The stability boundaries for the orthoclase-illite-kaolinite equilibriums are also
846 presented. The square represents constrained physicochemical conditions for stage II mineralization, and the
847 left and right boxes are the stability fields of calaverite and hessite at 280°C, (c): For stage III, at 240°C and
848 80 bars. Solid thick line is the stability field boundary for the equilibrium bornite + pyrite = chalcopyrite, at
849 240°C. Dotted, thicker dashed and dashed-dotted lines represent same as in (b). The stability boundary for
850 the albite-adularia equilibrium is also presented. The square represents constrained physicochemical
851 conditions for stage III mineralization, and the upper and lower boxes are the stability fields of calaverite and
852 hessite (after Zhang and Spry 1994), at 240°C, and (d): For stage IV, at 200°C and 50 bars. Dotted lines
853 represent the field boundaries of the principal aqueous sulfur species. Thicker dashed line represents the
854 stability field boundaries for pyrite and hematite. The dashed-dot-dotted lines are the $Au(HS)_2^-$ solubility
855 contours. The square represents physicochemical conditions for stage IV. All phase diagrams were
856 constructed assuming $m_{\sum S} = 0.01$ and $m_{K+} = 0.01$, and the thermodynamic data were derived from
857 SUPCRT92 database (Johnson 1992).
858 Fig. 16. LogfS_2 versus logfTe_2 equilibrium diagrams obtained from sulfides and tellurides at 280°C (a) and
859 240°C (b), at vapor saturation. The enclosed areas indicate the approximate physiochemical conditions of
860 stage II and III minerals precipitation. Diagrams are constructed based on data from Ahmad et al. (1987),
861 Afifi et al. (1988) and Simon and Essene (1996). Abbreviations: Bn-bornite, Cp-chalcopyrite, Po-pyrrhotite,
862 Py-pyrite, Te-native tellurium, $AuTe_2$-calaverite, Au-native gold, PbTe-altaite, PbS-galena, HgTe-coloradoite,
863 HgS-cinnabar, Hg-native mercury, Ag_2Te-hessite, Ag_2S-argentite.
864 Fig. 17. Plots of the solubility of calaverite (a) and hessite (b) as a function of $\alpha_{HS^-(aq)}$ and $\alpha_{HTe^-(aq)}$ at 280
865 and 240 °C. The star indicates an arbitrarily assumed starting composition, and three paths that could lead to
866 deposition of these minerals. Path1 could represent the result of sulfidation, whereas Path 2 could reflect the
867 condensation of a H_2Te vapor, and Path 3 a combination of the two proceses. The diagrams were constructed
868 using the program Unitherm (Shvarov 2011).

Zhai, D. G., A. E. Williams-Jones, J. J. Liu, S. F. Tombros, and N. J. Cook.
"Mineralogical, Fluid Inclusion, and Multiple Isotope (H-O-S-Pb) Constraints on the Genesis of the Sandaowanzi Epithermal Au-Ag-Te Deposit, Ne China."
Economic Geology 113, no. 6 (Sep 2018): 1359-82. http://dx.doi.org/10.5382/econgeo.2018.4595.

869

Zhai, D. G., A. E. Williams-Jones, J. J. Liu, S. F. Tombros, and N. J. Cook.
"Mineralogical, Fluid Inclusion, and Multiple Isotope (H-O-S-Pb) Constraints on the Genesis of the Sandaowanzi Epithermal Au-Ag-Te Deposit, Ne China."
Economic Geology 113, no. 6 (Sep 2018): 1359-82. http://dx.doi.org/10.5382/econgeo.2018.4595.

Table 1. Electron microprobe analyses of native metals, tellurides, sulfides and sulfosalts from the Sandaowanzi deposit

Mineral	1	1	2	3	4	5	6	6	7a	7b	8	9	9	10	11	12	13	14	15	16	17	18
Wt %																						
Se	0.01	0.01	0.25	0.27	0.24	0.16	0.10	0.09	0.01	bd	0.04	bd	bd	bd	bd	bd	bd	bd	0.33	bd	0.02	0.02
As	bd	bd	bd	bd	bd	bd	bd	bd	bd	bd	bd	3.48	4.37	21.06	bd	bd	bd	bd	bd	0.03	bd	bd
S	bd	bd	bd	bd	0.01	0.02	bd	bd	bd	bd	0.02	24.65	25.58	28.38	22.00	33.66	24.56	20.36	13.05	31.90	53.32	0.01
Pb	61.91	62.08	bd	bd	bd	bd	bd	bd	bd	bd	bd	0.22	0.12	0.00	bd	0.10	0.16	6.01	86.47	0.24	0.03	0.01
Bi	bd	bd	0.71	0.83	0.60	0.05	0.65	1.17	0.70	1.53	0.40	bd	0.01	0.09	0.04	bd	bd	bd	bd	bd	0.04	0.01
Ag	0.10	bd	5.63	0.81	6.07	62.59	4.01	4.04	12.21	6.64	47.84	bd	0.03	0.04	0.10	0.04	0.25	0.09	bd	bd	bd	0.02
Fe	0.03	0.04	bd	0.04	0.02	bd	bd	0.02	bd	bd	bd	0.27	0.19	3.02	2.00	30.29	10.44	3.40	0.03	0.29	46.78	0.12
Cu	0.12	bd	0.24	0.05	0.02	0.01	bd	0.01	bd	bd	bd	37.76	38.03	46.28	75.71	34.46	63.54	69.61	0.03	bd	0.10	59.33
Zn	bd	0.01	0.05	0.02	bd	bd	0.01	bd	bd	bd	0.01	7.63	7.45	2.48	0.06	0.08	0.03	0.06	0.02	65.65	0.00	40.69
Au	bd	0.05	32.48	40.88	38.16	0.03	68.03	72.16	85.93	90.95	19.45	0.02	0.00	0.12	0.05	0.06	0.02	0.13	0.00	0.02	bd	0.03
Te	37.45	38.46	59.37	58.01	55.74	38.01	25.98	22.02	0.08	0.14	34.06	bd	bd	bd	0.02	0.02	0.08	bd	0.14	bd	bd	0.01
Sb	bd	bd	bd	bd	bd	bd	bd	bd	bd	bd	bd	26.79	26.08	0.30	0.01	bd	bd	bd	bd	bd	0.01	bd
Ni	bd	bd	bd	bd	bd	bd	bd	bd	bd	bd	bd	bd	bd	bd	bd	bd	bd	bd	bd	bd	0.01	0.21
Co	bd	bd	bd	bd	bd	bd	bd	bd	0.02	bd	bd	bd	bd	0.01	bd	0.04	0.05	bd	bd	bd	0.04	bd
Total	99.60	100.65	98.72	100.90	100.85	100.86	98.78	99.51	98.95	99.26	101.81	100.82	101.85	101.78	99.98	98.73	99.12	99.66	100.06	98.14	100.33	100.44
Number of atoms based on																						
Se	0.00	0.00	0.03	0.02[d]	0.01[d]	0.01[e]	0.01[e]	0.01[e]	0.00	0.00	0.00	0.00	0.00	0.00	0.00	0.00	0.00	0.00	0.01[e]	0.00	0.00	0.00
As	0.00	0.00	0.00	0.00	0.00	0.00	0.00	0.00	0.00	0.00	0.00	0.77[h]	0.95[h]	3.96[g]	0.00	0.00	0.00	0.00	0.00	0.00	0.00	0.00
S	0.00	0.00	0.00	0.00	0.00	0.00	0.00	0.00	0.00	0.00	0.00	13.00	13.00	13.00	4.00	2.00	4.00	6.00	0.98[e]	0.99[n]	2.00	0.00
Pb	0.99[a]	0.99[a]	0.00	0.00	0.00	0.00	0.00	0.00	0.00	0.00	0.00	0.02[g]	0.01[g]	0.00	0.00	0.00	0.00	0.32[m]	1.00	0.00	0.00	0.00
Bi	0.00	0.00	0.06[b]	0.02[c]	0.01[c]	0.00	0.02[b]	0.03[b]	0.01[c]	0.01[c]	0.01[f]	0.00	0.00	0.01[g]	0.00	0.00	0.00	0.00	0.00	0.00	0.00	0.00
Ag	0.00	0.00	0.90[b]	0.03[c]	0.24[c]	2.00	0.19[b]	0.19[b]	0.20[c]	0.12[c]	3.27[f]	0.00	0.00	0.01[g]	0.01[i]	0.00	0.01[j]	0.01[l]	0.00	0.00	0.00	0.00
Fe	0.00	0.00	0.00	0.00	0.00	0.00	0.00	0.00	0.00	0.00	0.00	0.08[g]	0.06[g]	0.79[g]	0.22[i]	1.00	0.99[k]	0.68[m]	0.00	0.01[n]	1.00	0.01[o]
Cu	0.01[a]	0.01[a]	0.06[b]	0.00	0.00	0.00	0.00	0.00	0.00	0.00	0.00	9.93[g]	9.71[g]	10.61[g]	6.76[i]	1.00	4.99[j]	9.97[l]	0.00	0.00	0.00	2.99[o]
Zn	0.00	0.00	0.02[b]	0.00	0.00	0.00	0.00	0.00	0.00	0.00	0.00	1.97[g]	1.85[g]	0.55[g]	0.01[i]	0.00	0.00	0.01[l]	0.00	0.99	0.00	1.99[o]

Zhai, D. G., A. E. Williams-Jones, J. J. Liu, S. F. Tombros, and N. J. Cook.
"Mineralogical, Fluid Inclusion, and Multiple Isotope (H-O-S-Pb) Constraints on the Genesis of the Sandaowanzi Epithermal Au-Ag-Te Deposit, Ne China."
Economic Geology 113, no. 6 (Sep 2018): 1359-82. http://dx.doi.org/10.5382/econgeo.2018.4595.

Au	0.00	0.00	0.96[b]	0.92[c]	0.75[c]	0.00	1.79[b]	1.78[b]	0.79[c]	0.87[c]	1.00	0.00	0.00	0.01	0.00	0.00	0.00	0.01[l]	0.00	0.00	0.00	0.00
Te	1.00	1.00	4.03	1.98[d]	1.99[d]	0.99[e]	0.99[e]	0.99[e]	0.00	0.00	2.00	0.00	0.00	0.00	0.00	0.00	0.00	0.00	0.01[e]	0.00	0.00	0.00
Sb	0.00	0.00	0.00	0.00	0.00	0.00	0.00	0.00	0.00	0.00	0.00	3.64[h]	3.48[h]	0.04[h]	0.00	0.00	0.00	0.00	0.00	0.00	0.00	0.00
Ni	0.00	0.00	0.00	0.00	0.00	0.00	0.00	0.00	0.00	0.00	0.00	0.00	0.00	0.00	0.00	0.00	0.00	0.00	0.00	0.00	0.00	0.01[o]
Co	0.00	0.00	0.00	0.00	0.00	0.00	0.00	0.00	0.00	0.00	0.00	0.00	0.00	0.00	0.00	0.00	0.01[k]	0.00	0.00	0.00	0.00	0.00

[a]Pb+Cu = 1, Te = 1

[b]Ag + Au +Bi +Cu + Zn = 2, Te = 4

[c]Au + Ag + Bi = 1, [d]Te +Se = 2

[e]Te +Se + S = 1

[f]Ag + Bi = 3.28, Au = 1, Te = 2

[g]Cu + Zn + Fe + Pb + Ag + Bi = 2, [h] Sb + As = 2, S = 13

[i]Cu + Fe + Ag + Zn = 7, S = 4

[i]Cu + Fe + Ag + Zn = 7, S = 4

[j]Cu + Ag = 7, [k]Fe + Co = 1, S = 4

[l]Cu + Ag + Au + Zn = 10, [m]Pb + Fe = 1, S = 6

[n]Zn + Fe = 1, S = 1

[o]Cu + Zn + Ni + Fe = 6

1 = altaite from stage III (CM13/170m)

2 = sylvanite from stage III (CM13/170m)

3 = calaverite from stage III (CM23/130m)

4 = krennerite from stage III (CM23/130m)

5 = hessite from stage III (CM23/130m)

6 = unnamed telluride ($Au_{1.8}Ag_{0.2}Te$) from Stage III (CM23/130m)

7a = electrum from stage II (CM28/130m)

7b = native gold from stage III (CM17/90m)

8 = petzite from stage III (CM17/90m)

9 = Zn-tetrahedrite from stage III (CM13/170m)

10 = tennantite from stage III (CM13/170m)

11 = anilite from stage III (CM23/130m)

12 = chalcopyrite from stage II (CM28/130m)

13 = bornite from stage II (CM23/130m)

14 = betekhtinite from stage II (CM23/130m)

15 = galena from stage II (CM28/130m)

16 = sphalerite from stage II (CM28/130m) with X_{FeS} = 0.49%

17 = pyrite from stage I (CM37/90m)

18 = brass from stage III (CM28/130m)

Abbreviations: bd: Below detection limit and CM: The transverses drifts used at the mine.

Table 2. Microthermometric data of primary fluid inclusions in quartz veins from the Sandaowanzi deposit

Sample	Location	N	Stage	Mineral	Phases	Tm_{ice} (°C)	Th (°C)	Tm_{halite} (°C)	Salinity (wt.% NaCl equiv)
sdwz-12	279 line	22	I	Milky quartz	L-V and V-L	-2.5 to -0.3	240 to 385	-	0.53 to 4.18
sdwz-13	CM17/90m	30	I	Milky quartz	L-V and V-L	-2.1 to -0.6	256 to 381	-	1.05 to 3.55
sdwz-36	CM17/90m	30	II	Grey quartz	L-V and V-L	-3.6 to -0.2	230 to 345	-	0.35 to 5.86
sdwz-43	CM28/130m	17	II	Grey quartz	L-V and V-L	-10.2 to -0.2	160 to 400	-	0.35 to 14.15
sdwz-49	CM25/130m	49	II	Grey quartz	L-V and V-L	-1.8 to -0.4	177 to 306	-	0.70 to 3.06
sdwz-49-2	CM25/130m	4	II	Grey quartz	L-V-S	-	307 to 365	384 to 430	45.3 to 51.9
sdwz-52	CM33/130m	34	III	Clear quartz	L-V and V-L	-1.8 to -0.2	160 to 360	-	0.35 to 3.06
sdwz-47	CM23/130m	25	III	Clear quartz	L-V	-4.0 to -0.5	157 to 365	-	0.88 to 6.45
sdwz-48	CM23/130m	29	III	Clear quartz	L-V and V-L	-3.6 to -0.3	195 to 285	-	0.53 to 5.86
sdwz-56	CM28/50m	38	IV	White quartz	L-V and V-L	-3.2 to -0.1	128 to 243	-	0.18 to 5.26
sdwz-57	CM28/50m	21	IV	White quartz	L-V and V-L	-3.9 to -0.2	135 to 265	-	0.35 to 6.30

Tm_{ice} = final ice-melting temperature, Tm_{halite} = halite dissolution temperature, Th = homogenization temperature, - = not analyzed, N = the number of analyzed fluid inclusions.

Table 3. Compositions of vapor and liquid for fluid inclusions from the Sandaowanzi deposit (μg/g)

Sample	Mineral	CH_4	C_2H_2+ C_2H_4	C_2H_6	CO_2	H_2O	O_2	N_2	Na^+	K^+	Mg^{2+}	Ca^{2+}	F^-	Cl^-	Br^-	NO_3^-	SO_4^{2-}
sdwz-22	Milky quartz (stage I)	0.42	0.10	bd	97.43	545.28	11.21	60.61	1.77	6.86	1.55	24.07	1.38	0.72	bd	0.19	8.82
sdwz-27a	Milky quartz (stage I)	0.27	0.06	bd	80.18	282.69	10.92	57.48	1.40	bd	bd	36.12	0.28	0.97	bd	0.15	3.84
sdwz-35	Grey quartz (stage	0.47	0.11	bd	146.16	529.04	25.40	123.05	1.79	4.42	0.90	32.02	0.31	1.36	0.12	0.11	3.03
sdwz-43	Grey quartz (stage	0.79	0.21	0.01	139.49	535.26	10.75	67.27	2.92	7.11	0.32	1.92	0.20	1.32	bd	0.29	9.66
sdwz-36	Grey quartz (stage	0.40	0.14	0.01	164.44	291.05	22.32	113.98	2.26	11.93	0.76	28.74	0.28	0.98	bd	0.06	11.39
sdwz-47	Clear quartz (stage	0.27	0.12	0.01	84.33	432.31	13.74	70.32	1.84	4.54	0.24	13.32	0.68	0.52	0.07	0.10	6.65
sdwz-53	Clear quartz (stage	0.38	0.14	0.01	103.58	483.24	13.04	68.97	1.81	6.90	0.83	17.64	14.52	1.18	bd	0.10	3.08
sdwz-56	White quartz (stage	0.62	0.15	0.01	124.19	866.18	6.75	44.10	1.37	3.79	0.65	2.79	0.34	0.58	bd	0.06	8.24

Abbreviations: bd: Below detection limit

Zhai, D. G., A. E. Williams-Jones, J. J. Liu, S. F. Tombros, and N. J. Cook.
"Mineralogical, Fluid Inclusion, and Multiple Isotope (H-O-S-Pb) Constraints on the Genesis of the Sandaowanzi Epithermal Au-Ag-Te Deposit, Ne China."
Economic Geology 113, no. 6 (Sep 2018): 1359-82. http://dx.doi.org/10.5382/econgeo.2018.4595.

Table 4. Sulfur isotopic compositions of pyrite and chalcopyrite from the Sandaowanzi deposit

Sample	Location	Occurrence	Stage	Mineral	Temperature[A] (°C)	$\delta^{34}S_{CDT}$ (per mil)	$\delta^{34}S_{H2S}$[B] (per mil)
sdwz-26	CM13/170m	Trachyandesite	-	Pyrite	330	-0.5	-1.6
sdwz-38	CM37/90m	Trachyandesite	-	Pyrite	330	-0.4	-1.5
sdwz-39	238 line	Trachyandesite	-	Pyrite	330	0.3	-0.8
sdwz-55	CM35/130m	Trachyandesite	-	Pyrite	330	0.9	-0.2
sdwz-32	CM27/90m	Grey quartz	II	Pyrite	280	0.6	-0.7
sdwz-50	CM23/130m	Grey quartz	II	Pyrite	280	-0.9	-2.2
sdwz-43	CM28/130m	Grey quartz	II	Chalcopyrite	280	-1.8	-1.6
sdwz-47	CM23/130m	Clear quartz	III	Chalcopyrite	240	-2.2	-2.0

[A]Average homogenization temperatures of fluid inclusions from grey (stage II) and clear quartz (stage III)

[B]Utilizing H_2S-sulfide equations of Grootenboer and Schwarcz (1969) and Ohmoto and Rye (1979)

Table 5. Oxygen and hydrogen isotopic compositions for samples from the Sandaowanzi deposit

Sample	Location	Stage	Mineral/Rock	Temperature[A] (°C)	$\delta^{18}O_{SMOW}$ (per mil)	$\delta^{18}O_{H2O}$[B] (per mil)	δD_{H2O} (per mil)
sdwz-22	CM7/170m	I	Milky quartz	330	-2.5	-10.6	-123
sdwz-35	CM15/90m	II	Grey quartz	280	-0.4	-8.3	-116
sdwz-53	CM33/130m	II	Grey quartz	280	-0.3	-10.1	-111
sdwz-36	CM17/90m	II	Grey quartz	280	-1.9	-9.7	-98
sdwz-47	CM23/130m	III	Clear quartz	240	-3.3	-12.9	-107
sdwz-27a	CM13/170m	III	Clear quartz	240	-1.8	-9.8	-96
sdwz-04	296 line	III	Clear quartz	240	-3.9	-12.0	-123
sdwz-43	CM28/130m	III	Clear quartz	240	-0.3	-7.6	-101
sdwz-56	CM33/50m	IV	White quartz	200	-3.5	-13.6	-109
sdwz-58	CM35/50m	IV	White quartz	200	-2.6	-10.9	-127

[A]Average homogenization temperatures from milky (stage I), grey (stage II), clear (stage III) and white quartz (stage IV) and the maximum temperature obtained from fluid inclusions

[B]Utilizing the quartz-H_2O equations of Zheng (1993)

Table 6. Lead isotope ratios for pyrite, the host trachyandesite and monzogranite from the Sandaowanzi deposit

Sample	Mineral/Rock	$^{208}Pb/^{204}Pb$	$^{207}Pb/^{204}Pb$	$^{206}Pb/^{204}Pb$	$^{208}Pb/^{206}Pb$	$^{207}Pb/^{206}Pb$
09sdwz-26	Pyrite	38.0901	15.5404	18.2366	2.0887	0.8522
09sdwz-32	Pyrite	38.2293	15.5624	18.3146	2.0873	0.8497
09sdwz-38	Pyrite	38.1919	15.557	18.3119	2.0856	0.8496
09sdwz-39	Pyrite	38.0982	15.5409	18.2433	2.0884	0.8519
09sdwz-50	Pyrite	38.1499	15.5465	18.2776	2.0873	0.8506
09sdwz-55	Pyrite	38.1863	15.555	18.2726	2.0898	0.8513
09sdwz-61	Monzogranite	38.2882	15.5658	18.2729	2.0954	0.8519
09sdwz-62	Monzogranite	38.6944	15.5863	18.8377	2.0541	0.8274
09sdwz-55(2)	Trachyandesite	38.2400	15.6255	18.2138	2.0995	0.8579
09sdwz-26(2)	Trachyandesite	38.2066	15.5487	18.3296	2.0844	0.8483
09sdwz-38(2)	Trachyandesite	38.2277	15.6188	18.2093	2.0994	0.8577

All errors are reported at ±2σ (minimum of 0.00001 and maximum of 0.0035)

Table 7. Calculated physicochemical parameters of the Sandaowanzi mineralizing fluid

Physicochemical Parameter	Stage I	Stage II	Stage III	Stage IV
pH	3.0 to 3.2	4.0 to 4.3	4.5 to 5.1	5.9 to 6.0
$\log(\alpha_{K^+}/\alpha_{H^+})$	3.7	2.3	4.9	-
$\log(\alpha_{Na^+}/\alpha_{H^+})$	2.4	4.0 to 4.4	5.9	-
$\log[\alpha_{Ca^{++}}/(\alpha_{H^+})^2]$	5.1	6.0	9.5	-
$\log[\alpha_{Mg^{++}}/(\alpha_{H^+})^2]$	4.3	6.8	5.2 to 5.3	-
$\log f_{S2}$	-9.5 to -8.4	-12.1 to -9.2	-14.1 to -10.6	-
$\log f_{Te2}$	-	-12.6 to -9.9	-15.2 to -7.9	-
$\Delta\log fO_2$ (HM)	-2.6 to -2.2	-2.1 to -1.0	-0.6 to -0.4	+1.9
$\log f_{H2S(g)}$	-0.9 to -0.1	-1.5 to -1.4	-2.6 to -1.8	-
$\log\alpha_{H2S(aq)}$	-3.2	-4.0	-4.3	-
$\log\alpha_{HS^-(aq)}$	-1.7 to -1.6	-1.6 to -1.2	-1.3 to -1.2	-
$\log f_{H2S(g)}/f_{SO2(g)}$	-10.7 to -10.3	-12.1 to -11.0	-7.8 to -8.6	5.3
$\log f_{H2Te(g)}$	-	-2.1 to -1.7	-1.6 to -1.5	-
$\log\alpha_{H2Te(aq)}$	-	-5.6 to -4.4	-3.9 to -3.5	-
$\log\alpha_{HTe^-(aq)}$	-	-3.8 to -3.6	-1.7 to -1.5	-
$\log f_{H2S(g)}/f_{H2Te(g)}$	-	0.6 to 0.3	-0.3 to -1.0	-
$\log\alpha Au(HS)_{2(aq)}^-$	-13.4 to -13.0	-11.4 to -10.6	-9.7 to -9.3	-9.1 to -8.8
$\log\alpha Fe^{++}_{(aq)}$	-3.7 to -3.5	-5.8 to -5.2	-	-
$\log\alpha Zn^{++}_{(aq)}$	-9.10	-7.80	-	-
$\log\alpha Cu(HS)_{2^-(aq)}$	-8.5 to -8.4	-7.3 to -7.1	-	-
$\log\alpha Pb^{++}_{(aq)}$	-	-3.9 to -3.7	-4.2 to -4.2	-

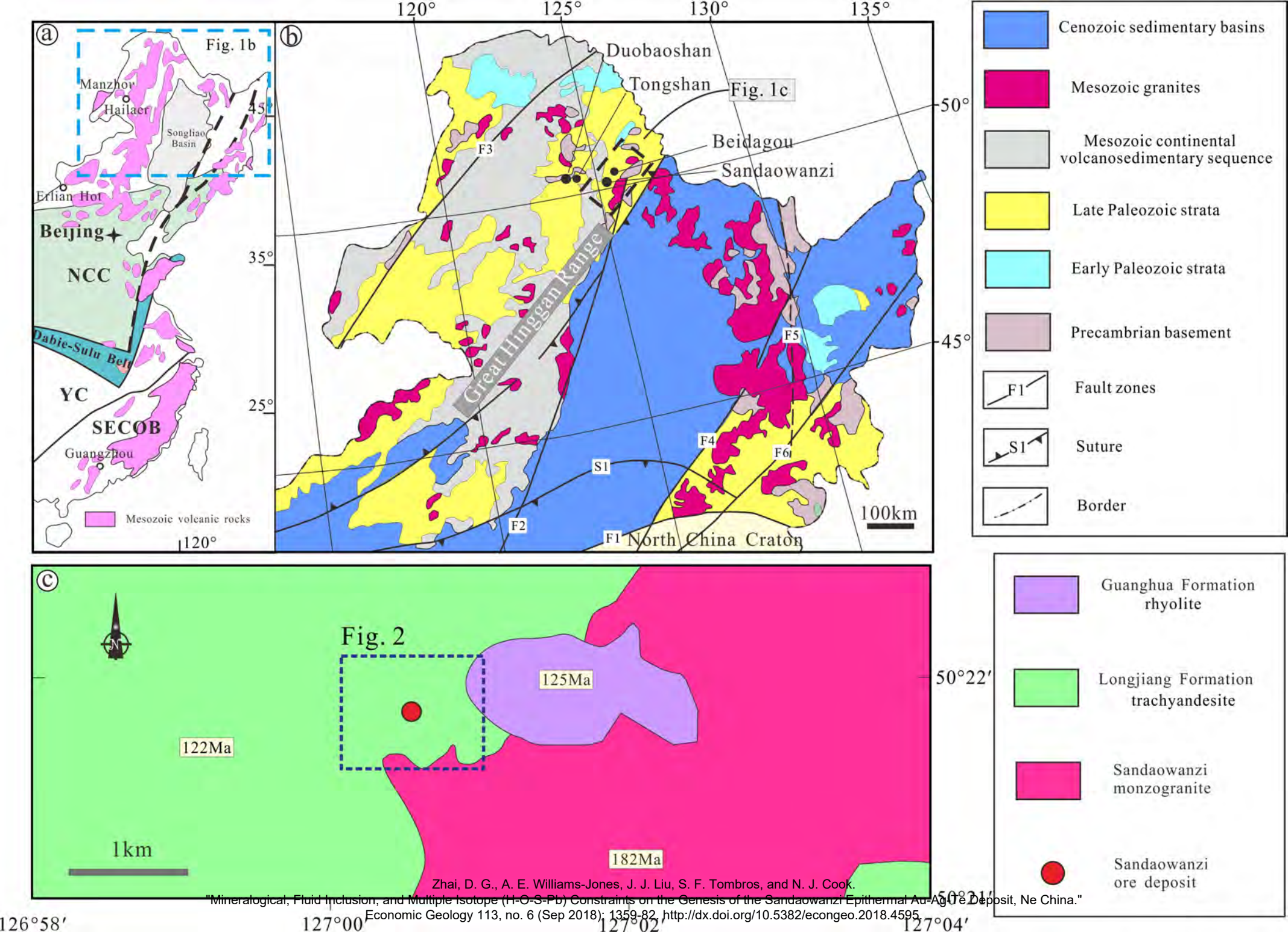

Zhai, D. G., A. E. Williams-Jones, J. J. Liu, S. F. Tombros, and N. J. Cook.
"Mineralogical, Fluid Inclusion, and Multiple Isotope (H-O-S-Pb) Constraints on the Genesis of the Sandaowanzi Epithermal Au-Ag-Te Deposit, Ne China."
Economic Geology 113, no. 6 (Sep 2018): 1359-82. http://dx.doi.org/10.5382/econgeo.2018.4595

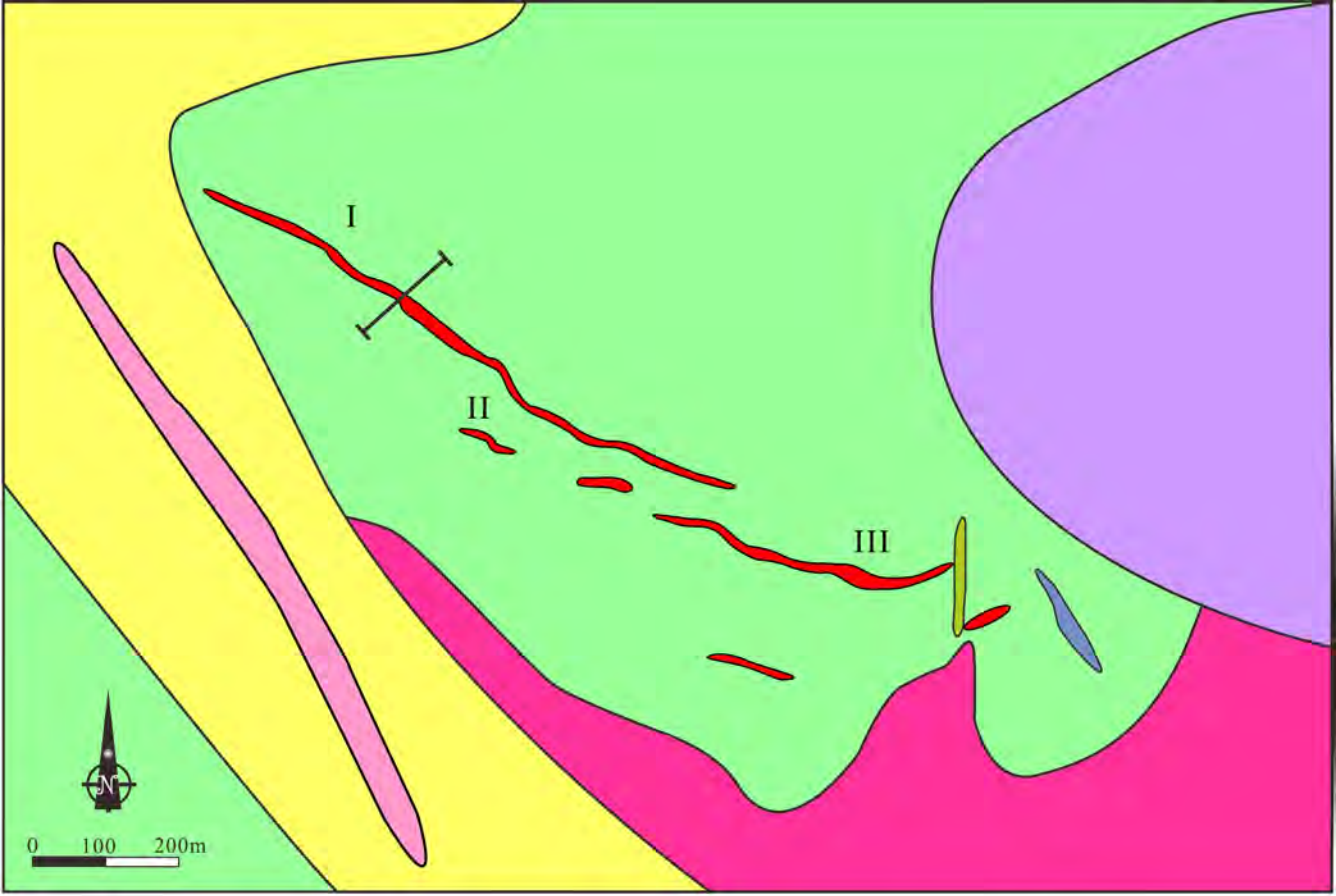

Quaternary gravel

Guanghua Formation rhyolite

Longjiang Formation trachyandesite

Sandaowanzi monzogranite

Diabase dike

Rhyolite porphyry

Metalliferous quartz vein

Placer gold ore body

Zhai, D. G., A. E. Williams-Jones, J. J. Liu, S. F. Tombros, and N. J. Cook.
alegical, Fluid Inclusion, and Multiple Isotope (H-O-S-Pb) Constraints on the Genesis of the Sandaowanzi Epithermal Au-Ag-Te Deposit, Ne C
Economic Geology 113, no. 6 (Sep 2018): 1359-82. http://dx.doi.org/10.5382/econgeo.2018.4595

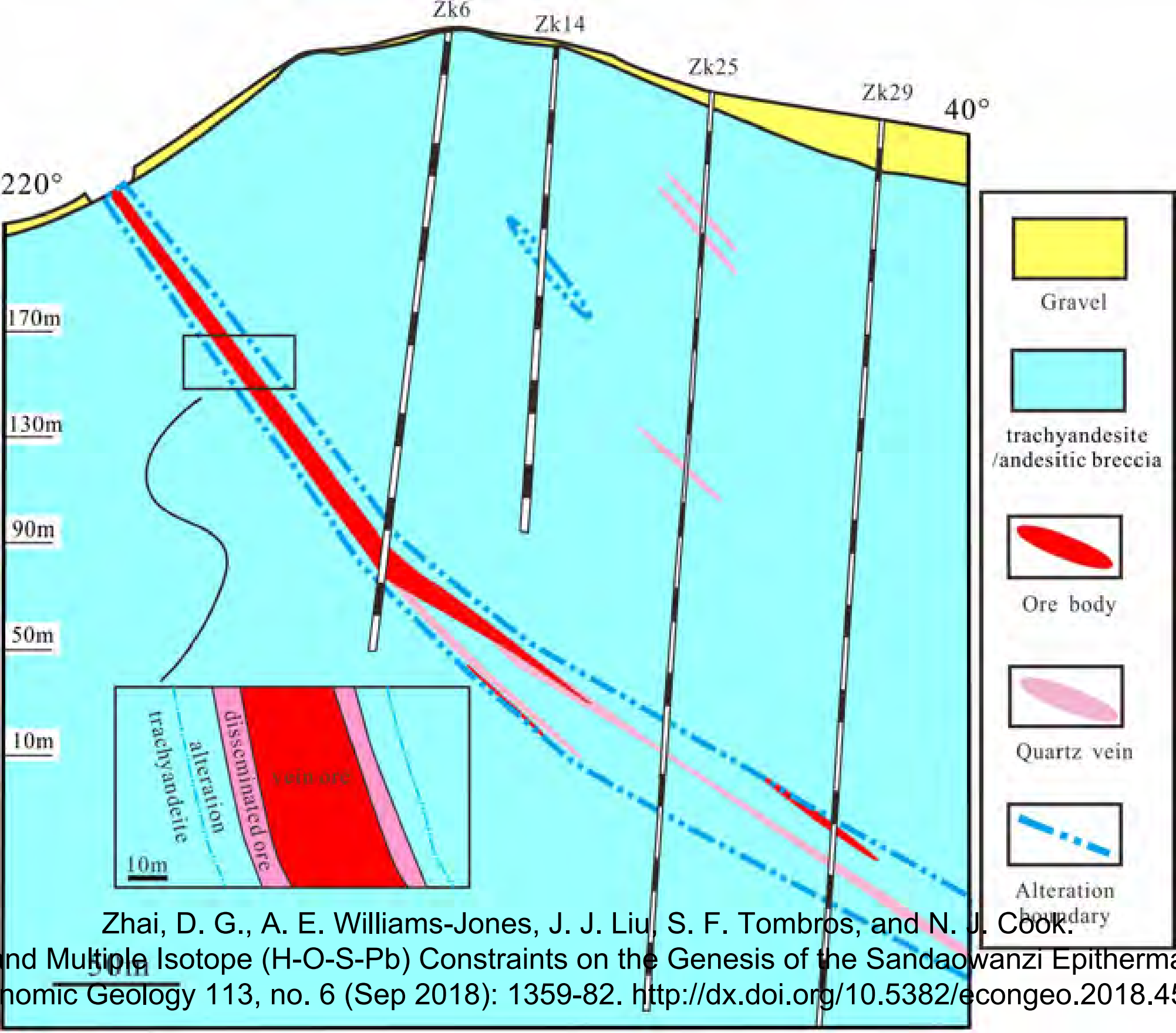

Zhai, D. G., A. E. Williams-Jones, J. J. Liu, S. F. Tombros, and N. J. Cook.
nd Multiple Isotope (H-O-S-Pb) Constraints on the Genesis of the Sandaowanzi Epitherma
nomic Geology 113, no. 6 (Sep 2018): 1359-82. http://dx.doi.org/10.5382/econgeo.2018.45

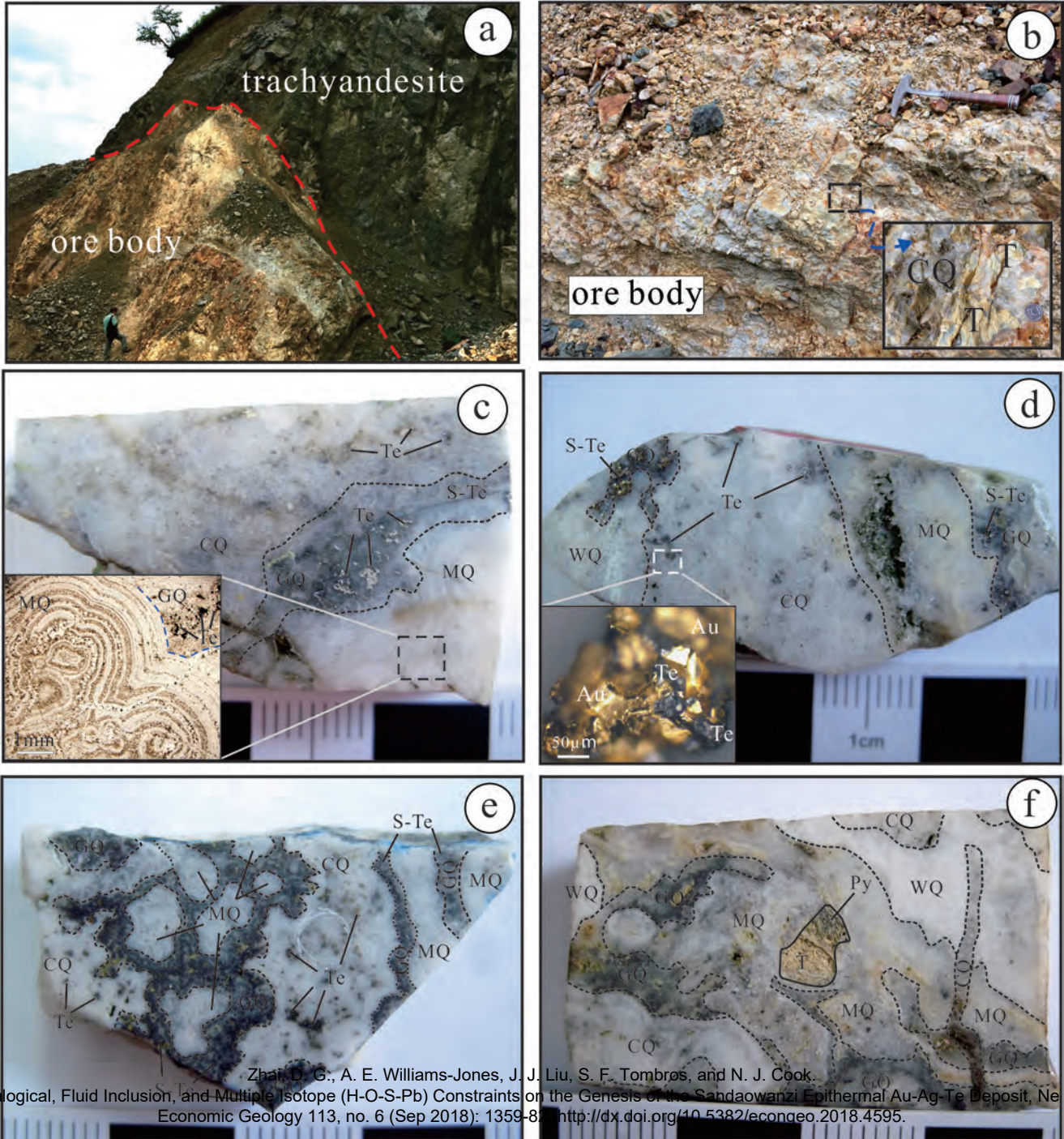

Zhai, D. G., A. E. Williams-Jones, J. J. Liu, S. F. Tombros, and N. J. Cook.
logical, Fluid Inclusion, and Multiple Isotope (H-O-S-Pb) Constraints on the Genesis of the Sandaowanzi Epithermal Au-Ag-Te Deposit, Ne
Economic Geology 113, no. 6 (Sep 2018): 1359-8 http://dx.doi.org/10.5382/econgeo.2018.4595.

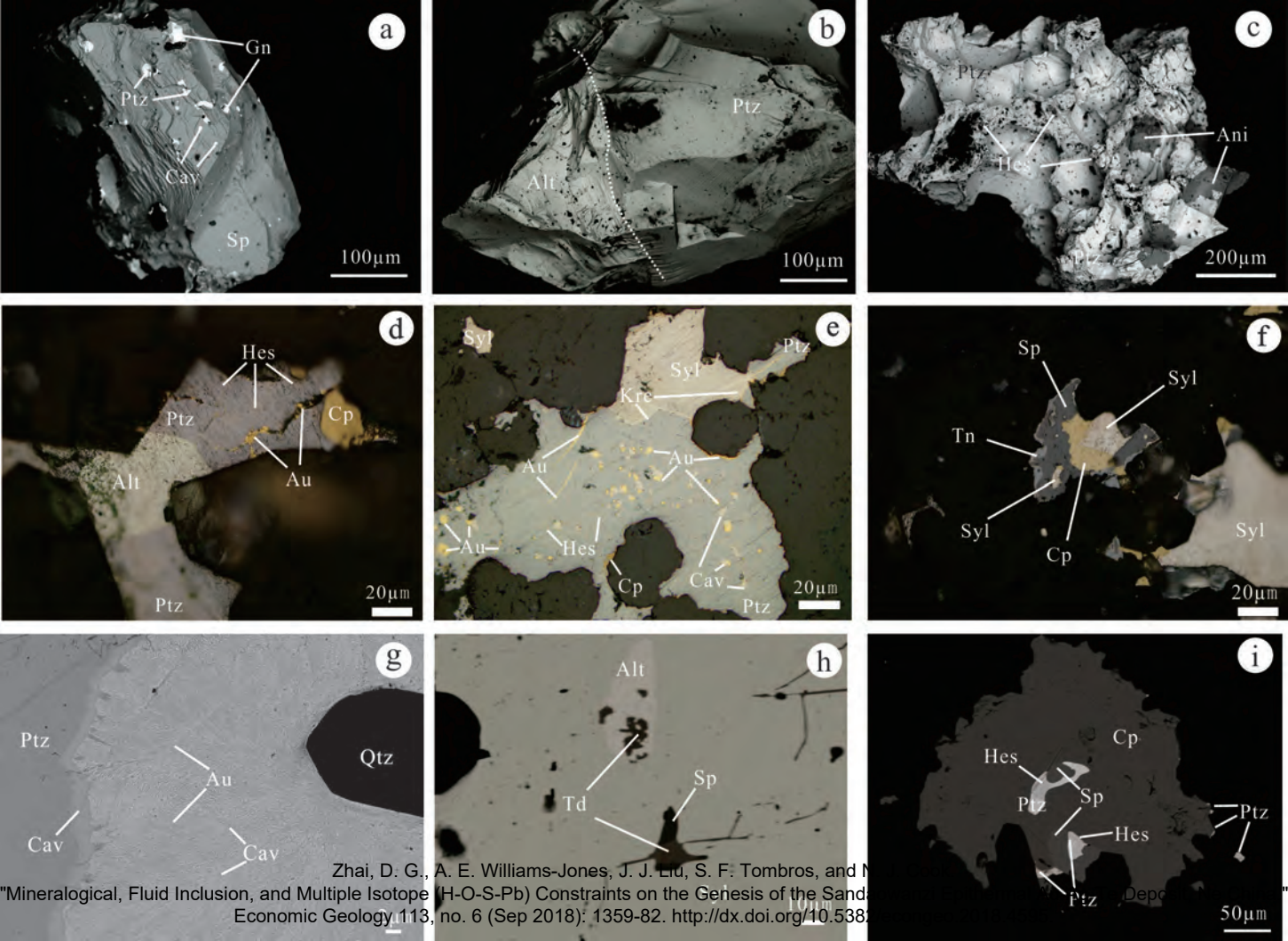

Zhai, D. G., A. E. Williams-Jones, J. J. Liu, S. F. Tombros, and N
"Mineralogical, Fluid Inclusion, and Multiple Isotope (H-O-S-Pb) Constraints on the Genesis of the Sand
Economic Geology 113, no. 6 (Sep 2018): 1359-82. http://dx.doi.org/10.538

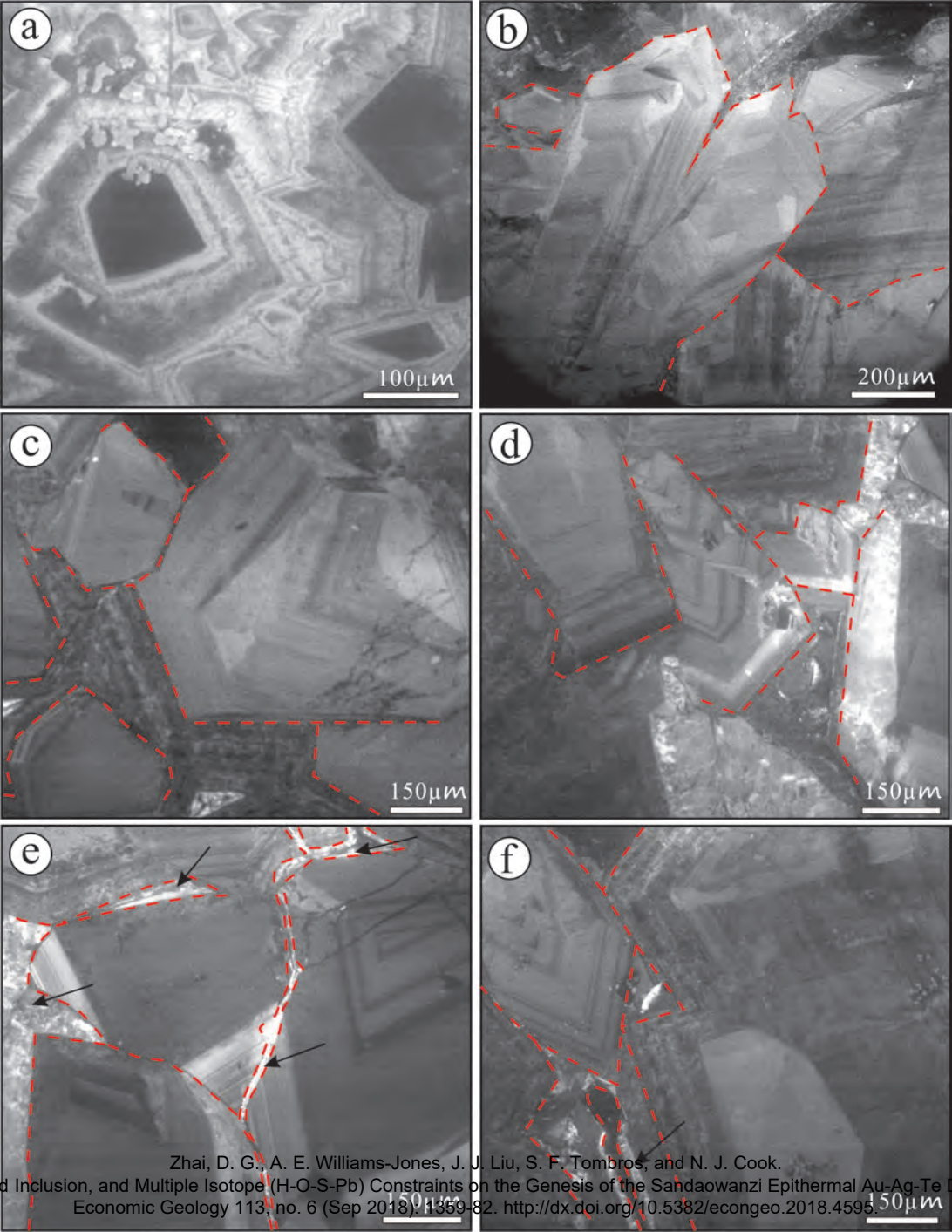

Zhai, D. G., A. E. Williams-Jones, J. J. Liu, S. F. Tombros, and N. J. Cook.
d Inclusion, and Multiple Isotope (H-O-S-Pb) Constraints on the Genesis of the Sandaowanzi Epithermal Au-Ag-Te D
Economic Geology 113, no. 6 (Sep 2018): 1359-82. http://dx.doi.org/10.5382/econgeo.2018.4595.

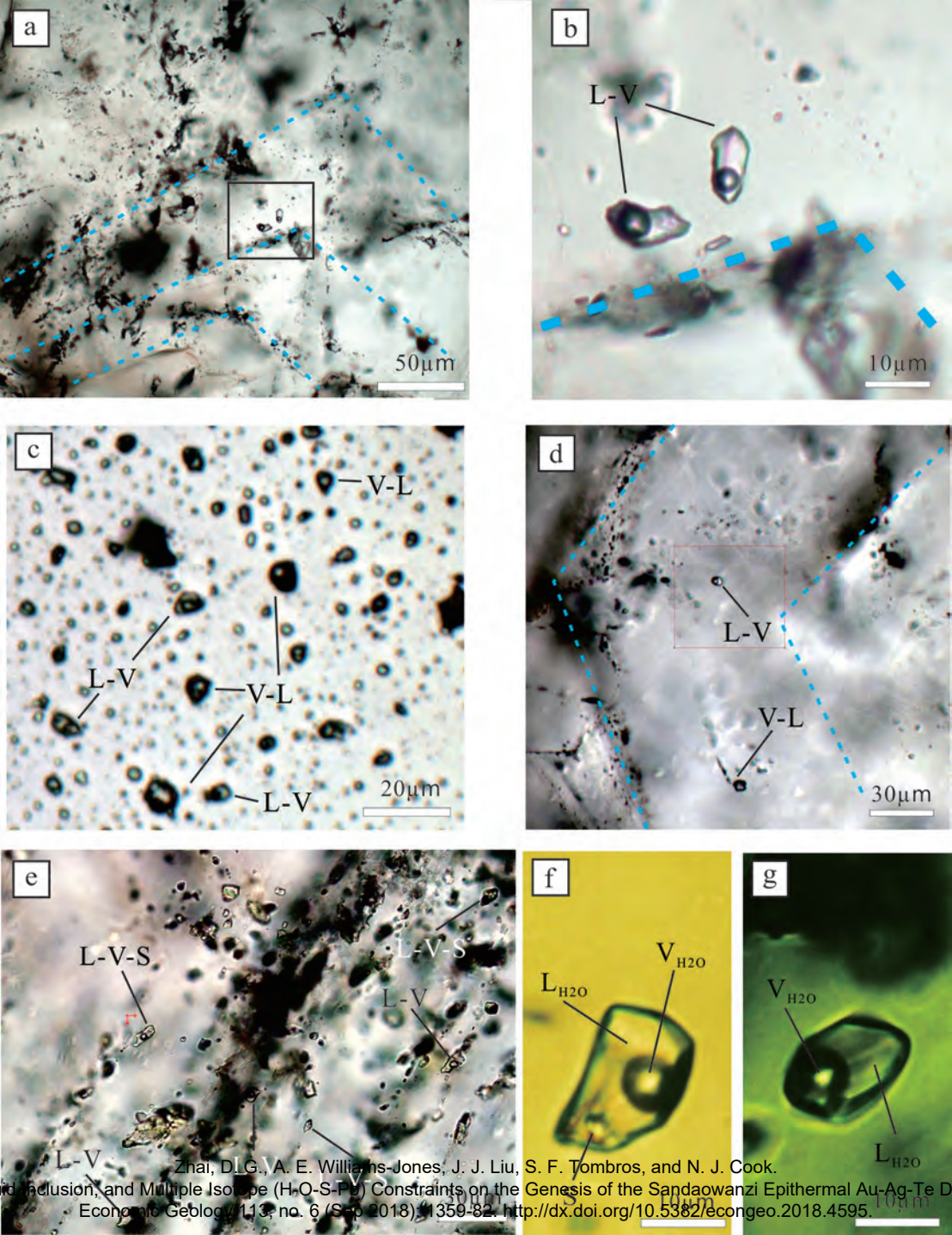

Zhai, D.G., A. E. Williams-Jones, J. J. Liu, S. F. Tombros, and N. J. Cook.
id Inclusion, and Multiple Isotope (H-O-S-Pb) Constraints on the Genesis of the Sandaowanzi Epithermal Au-Ag-Te D
Economic Geology 113, no. 6 (Sep 2018): 1359-82. http://dx.doi.org/10.5382/econgeo.2018.4595.

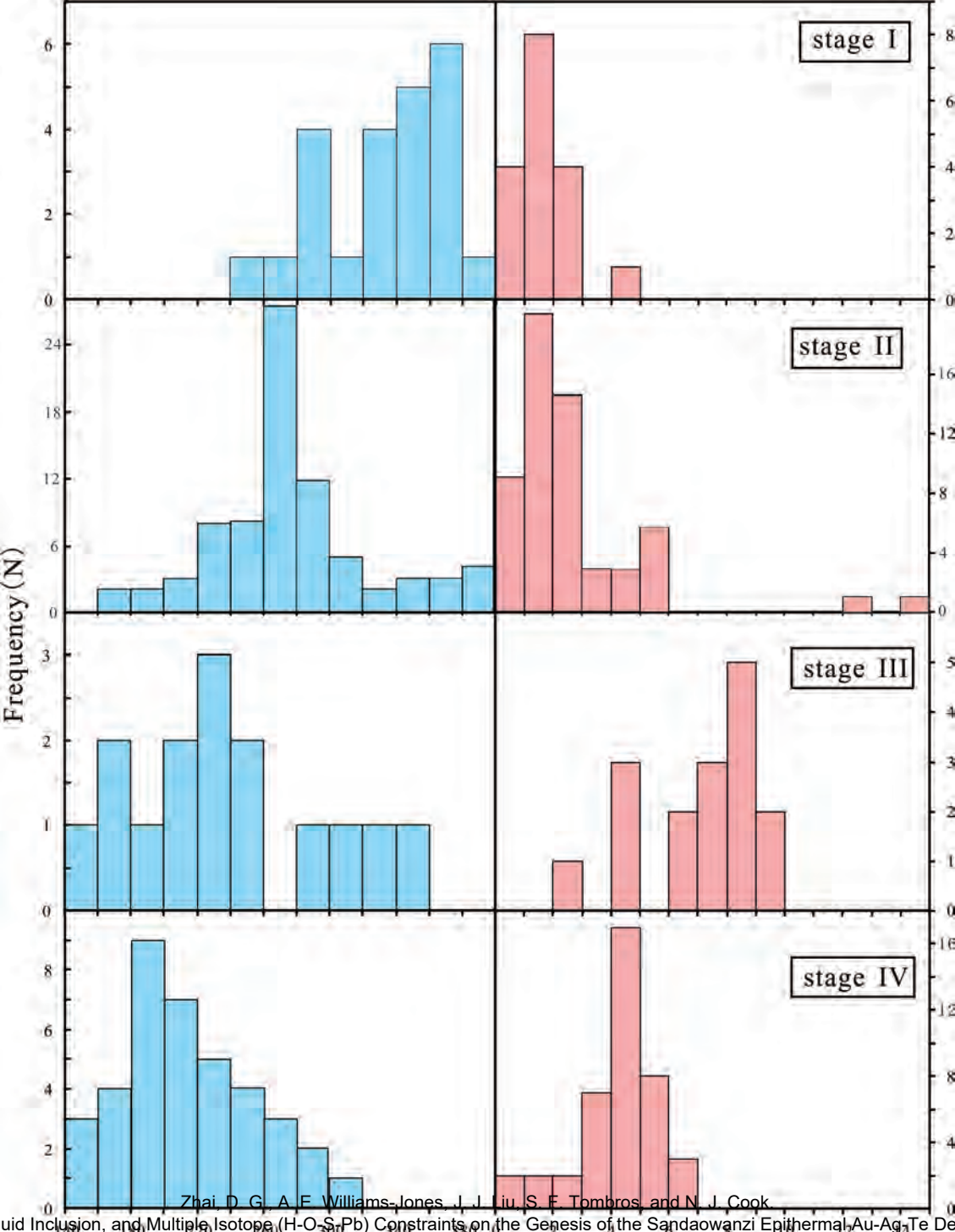

Zhai, D. G., A. E. Williams-Jones, J. J. Liu, S. F. Tombros, and N. J. Cook.
uid Inclusion, and Multiple Isotope (H-O-S-Pb) Constraints on the Genesis of the Sandaowanzi Epithermal Au-Ag-Te De
Economic Geology 113, no. 6 (Sep 2018): 1359-82. http://dx.doi.org/10.5382/econgeo.2018.4595.

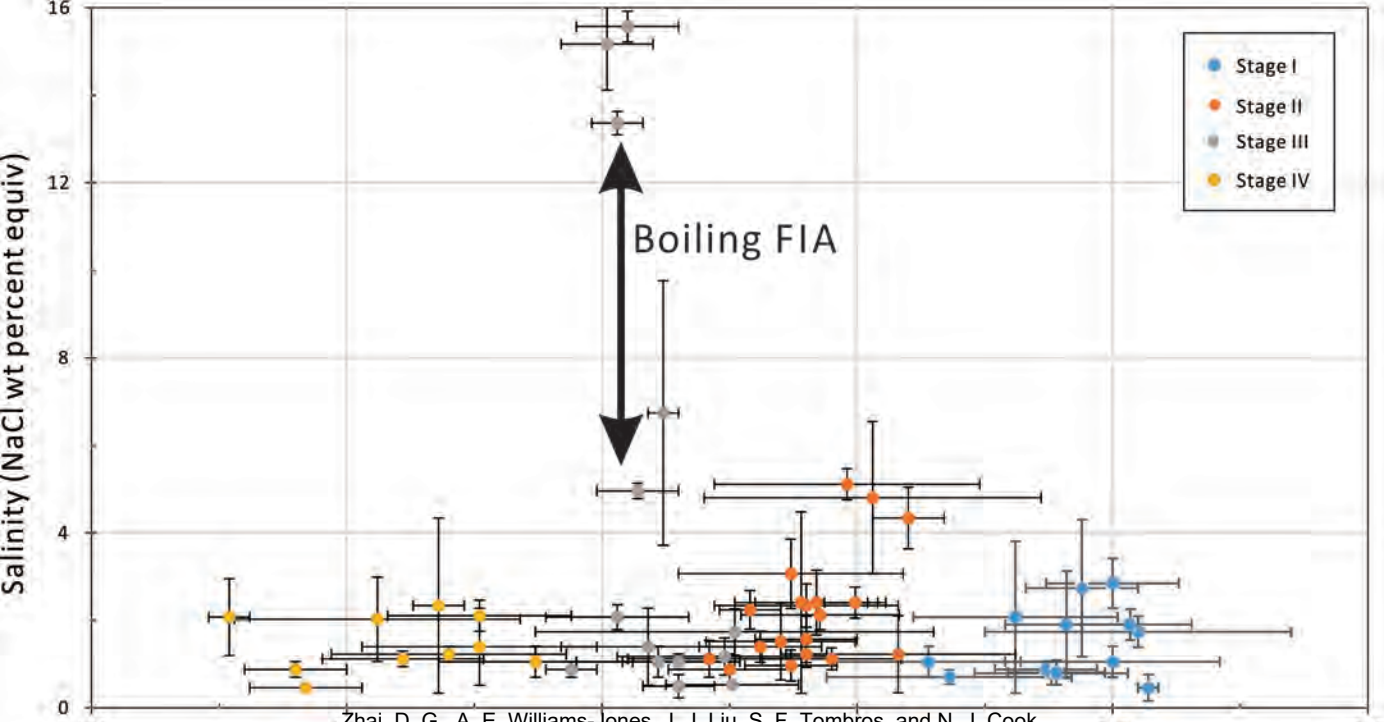

Zhai, D. G., A. E. Williams-Jones, J. J. Liu, S. F. Tombros, and N. J. Cook.
neralogical, Fluid Inclusion, and Multiple Isotope (H-O-S-Pb) Constraints on the Genesis of the Sandaowanzi Epithermal Au-Ag-Te Deposit, Ne Chi
Economic Geology 113, no. 6 (Sep 2018): 1359-82. http://dx.doi.org/10.5382/econgeo.2018.4595.

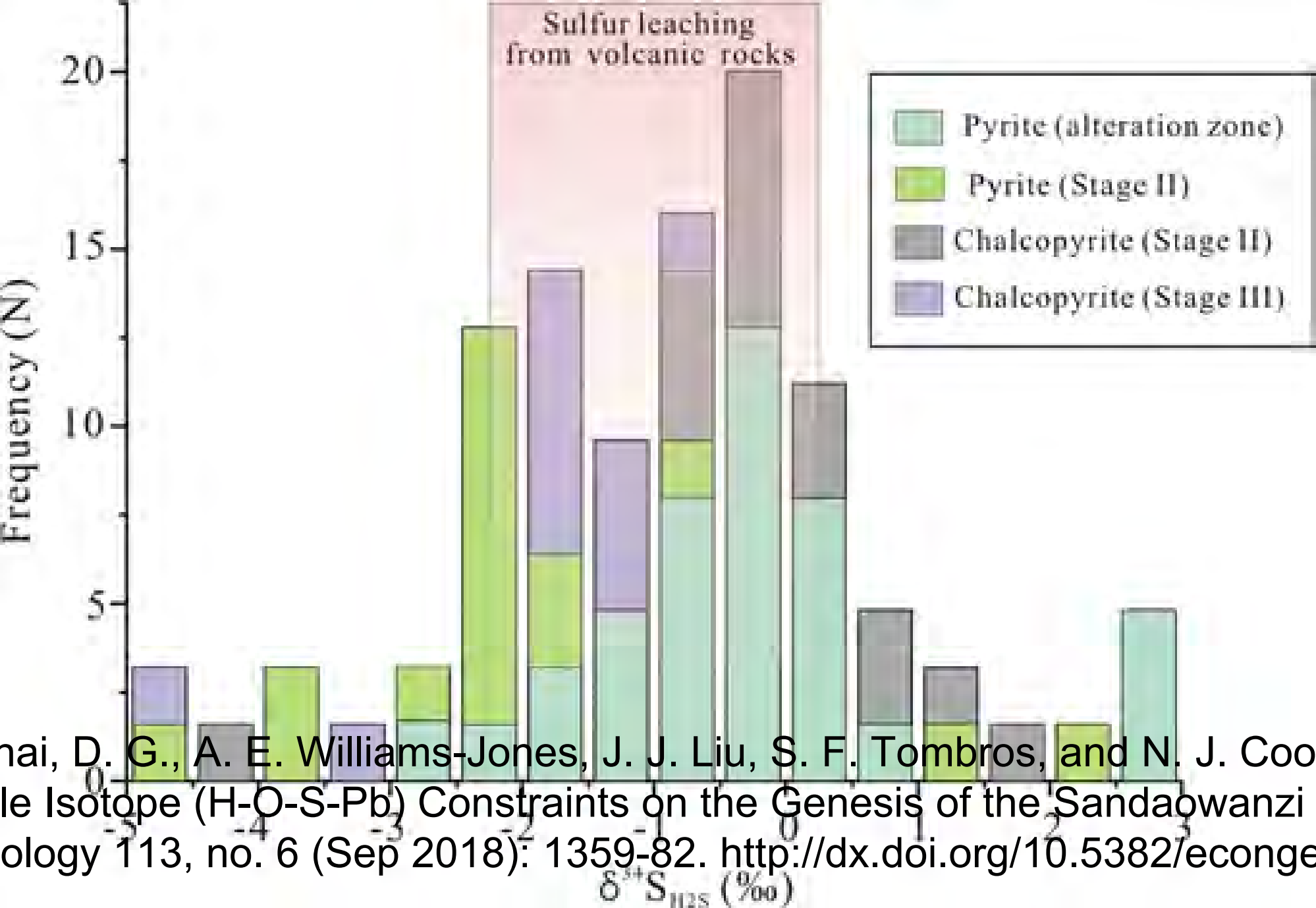

hai, D. G., A. E. Williams-Jones, J. J. Liu, S. F. Tombros, and N. J. Coo
le Isotope (H-O-S-Pb) Constraints on the Genesis of the Sandaowanzi
ology 113, no. 6 (Sep 2018): 1359-82. http://dx.doi.org/10.5382/econge

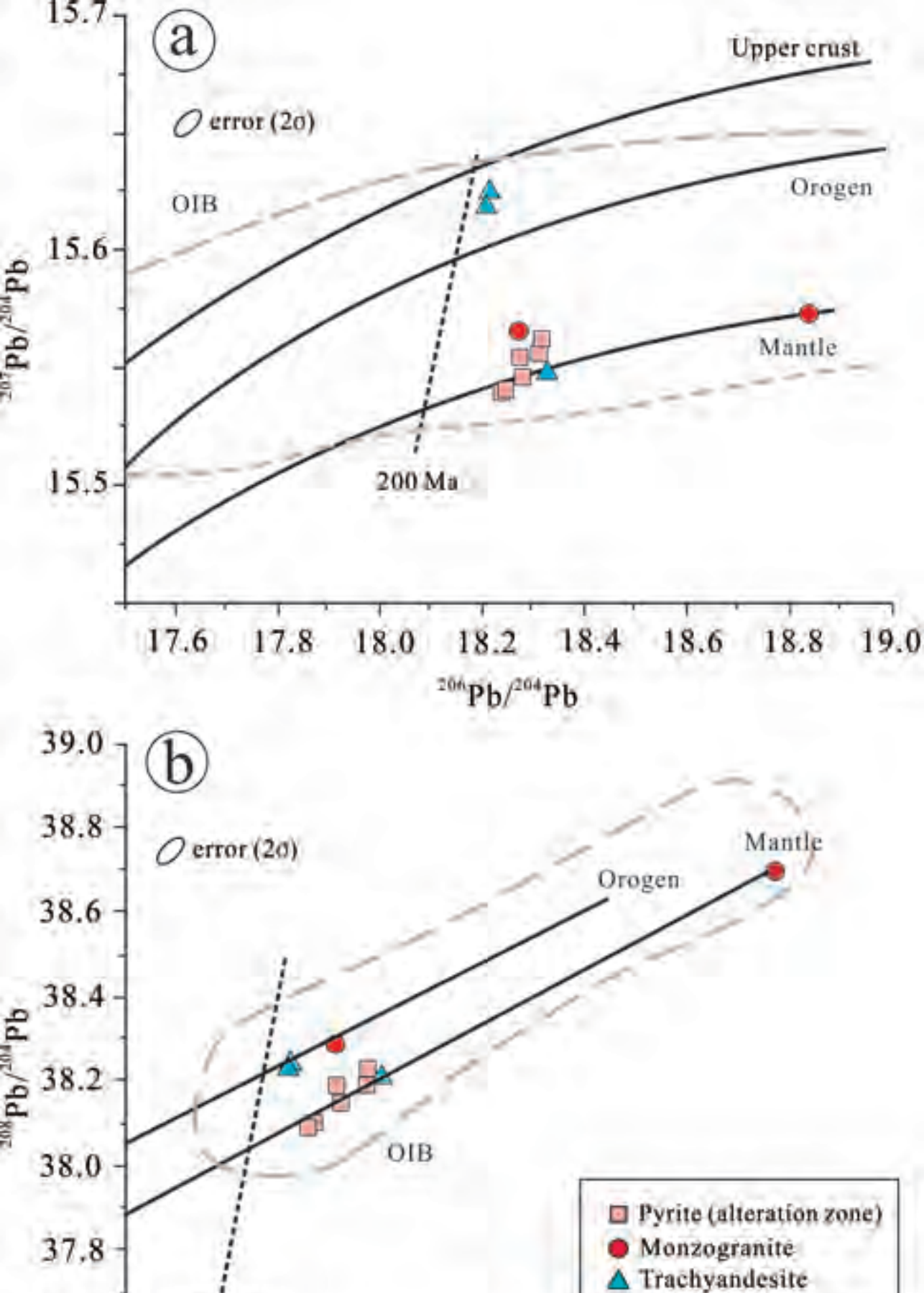

, D. G., A. E. Williams-Jones, J. J. Liu, S. F. Tombros, and N. J. C
Isotope (H-O-S-Pb) Constraints on the Genesis of the Sandaowan
ogy 113, no. 6 (Sep 2018): 1359-82. http://dx.doi.org/10.5382/econ

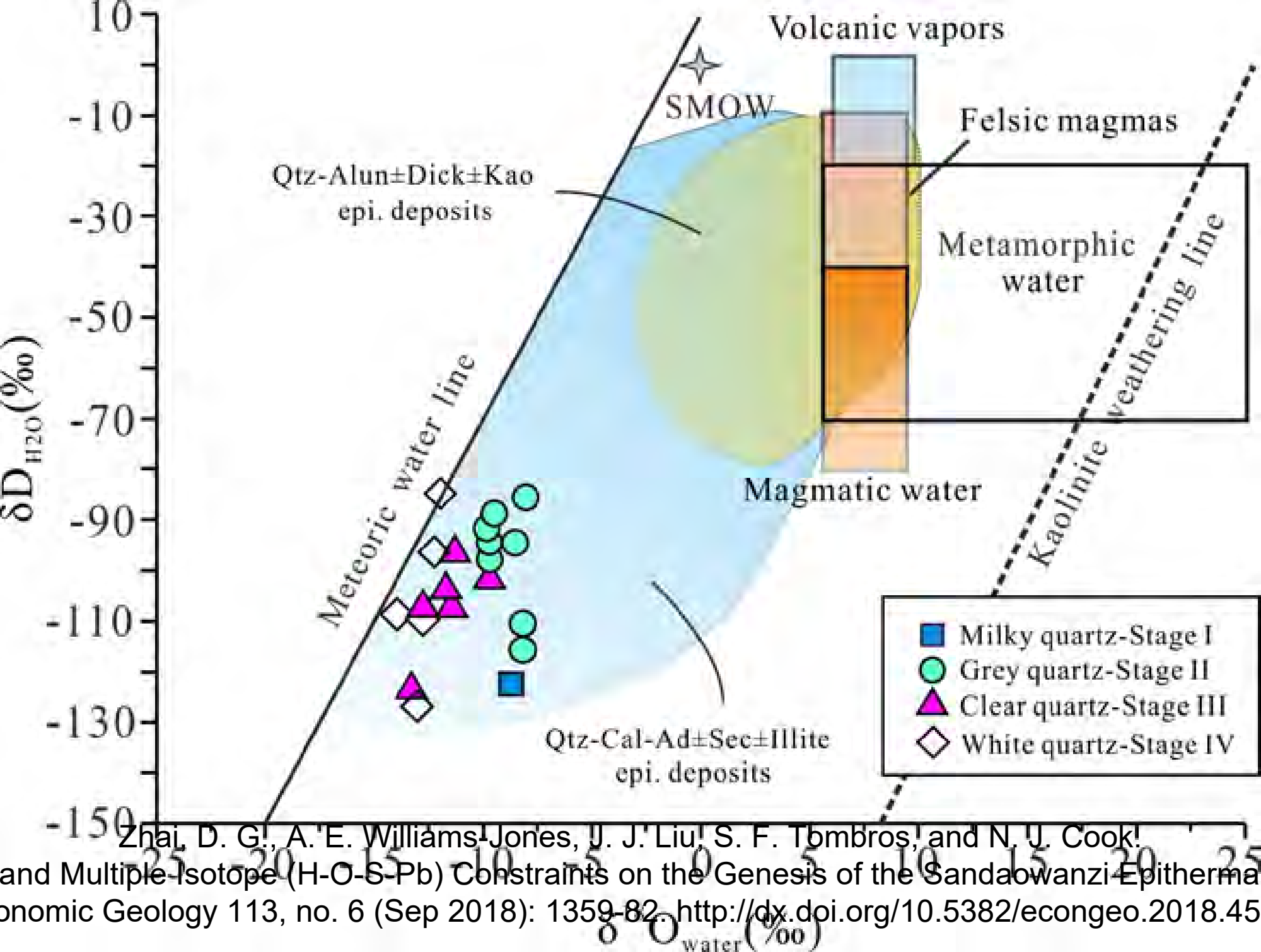

Zhai, D. G.; A. E. Williams-Jones, J. J. Liu, S. F. Tombros, and N. J. Cook. and Multiple-Isotope (H-O-S-Pb) Constraints on the Genesis of the Sandaowanzi Epitherma onomic Geology 113, no. 6 (Sep 2018): 1359-82. http://dx.doi.org/10.5382/econgeo.2018.45

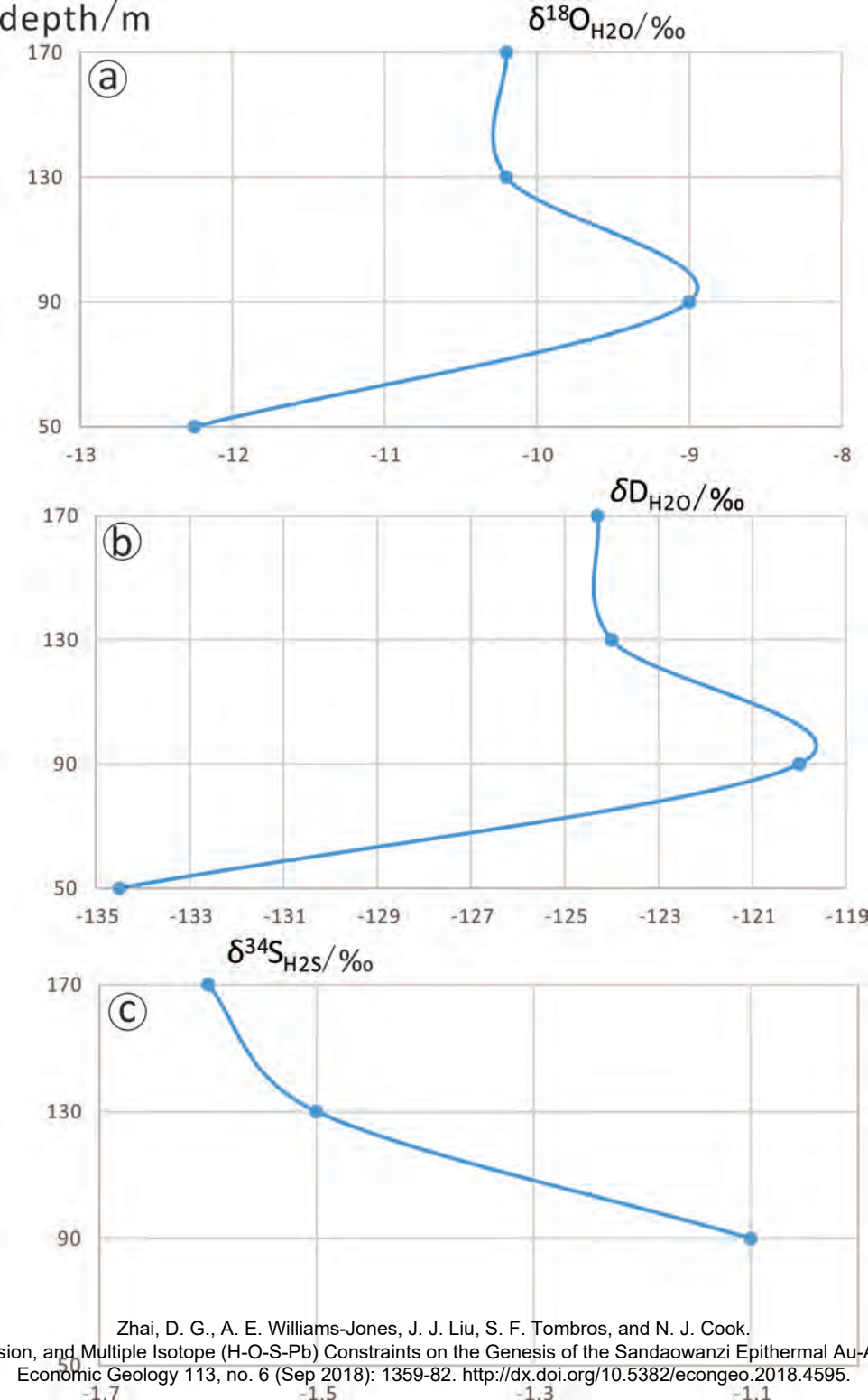

Zhai, D. G., A. E. Williams-Jones, J. J. Liu, S. F. Tombros, and N. J. Cook.
sion, and Multiple Isotope (H-O-S-Pb) Constraints on the Genesis of the Sandaowanzi Epithermal Au-A
Economic Geology 113, no. 6 (Sep 2018): 1359-82. http://dx.doi.org/10.5382/econgeo.2018.4595.

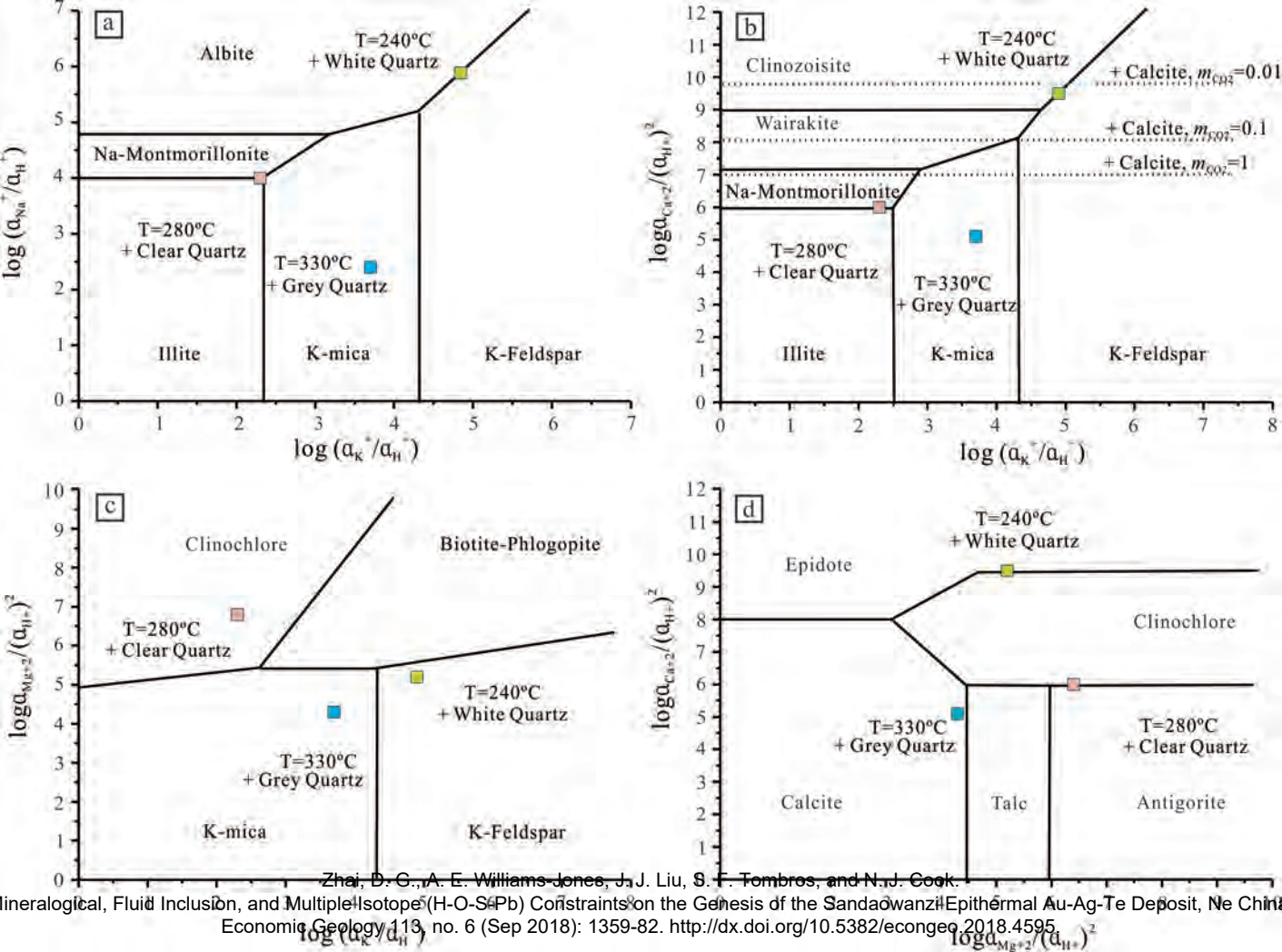

Zhai, D. G., A. E. Williams-Jones, J. J. Liu, S. F. Tombros, and N.J. Cook. Mineralogical, Fluid Inclusion, and Multiple Isotope (H-O-S-Pb) Constraints on the Genesis of the Sandaowanzi Epithermal Au-Ag-Te Deposit, NE China. Economic Geology 113, no. 6 (Sep 2018): 1359-82. http://dx.doi.org/10.5382/econgeo.2018.4595

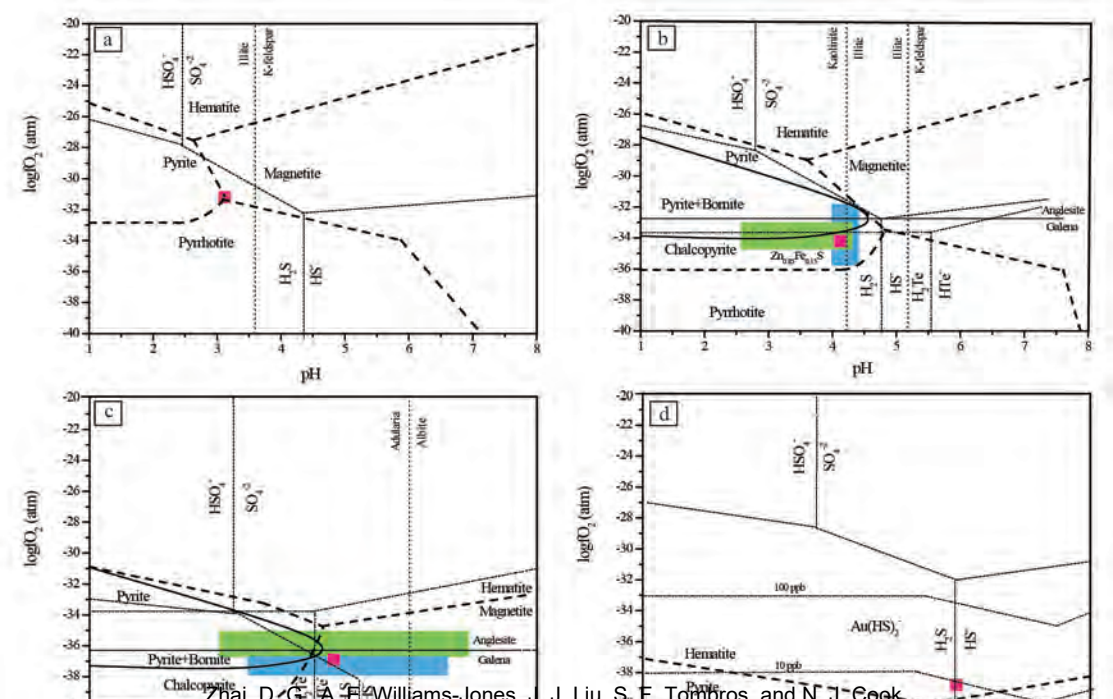

Zhai, D. G., A. E. Williams-Jones, J. J. Liu, S. F. Tombros, and N. J. Cook.
uid Inclusion, and Multiple Isotope (H-O-S-Pb) Constraints on the Genesis of the Sandaowanzi Epithermal Au-Ag-Te D
Economic Geology 113, no. 6 (Sep 2018): 1359-82. http://dx.doi.org/10.5382/econgeo.2018.4595.

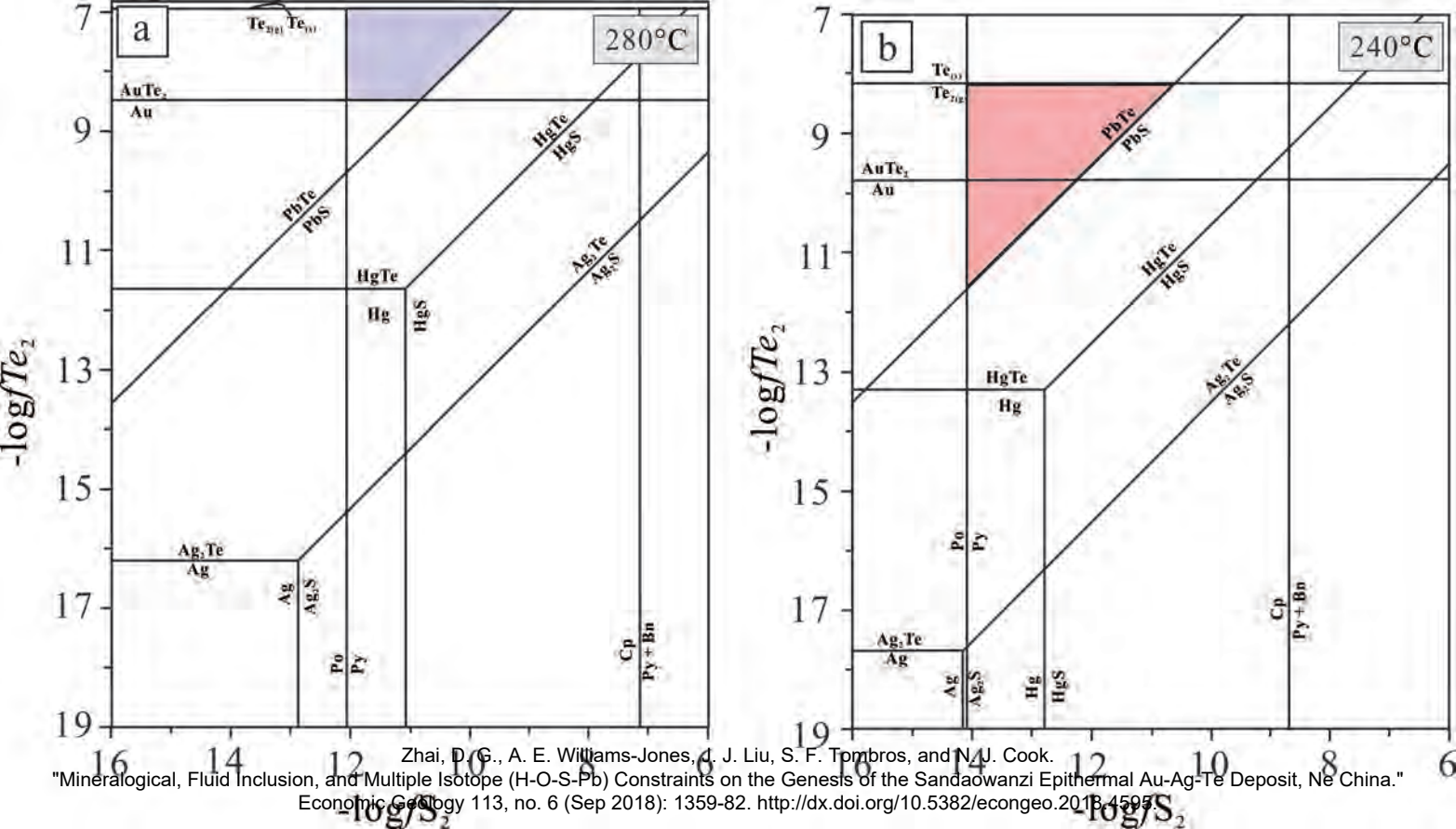

Zhai, D. G., A. E. Williams-Jones, J. J. Liu, S. F. Tombros, and N. J. Cook. "Mineralogical, Fluid Inclusion, and Multiple Isotope (H-O-S-Pb) Constraints on the Genesis of the Sandaowanzi Epithermal Au-Ag-Te Deposit, NE China." Economic Geology 113, no. 6 (Sep 2018): 1359-82. http://dx.doi.org/10.5382/econgeo.2018.4593

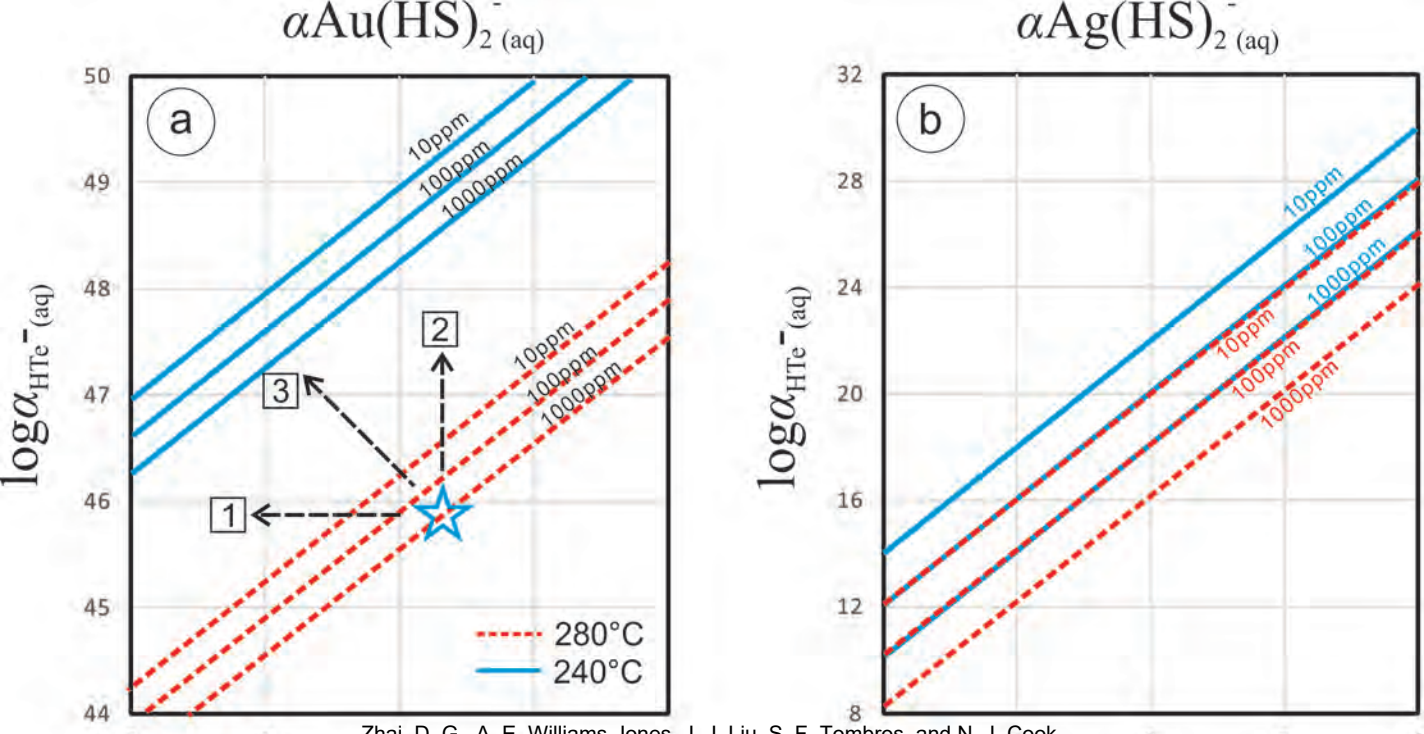

Zhai, D. G., A. E. Williams-Jones, J. J. Liu, S. F. Tombros, and N. J. Cook.
Mineralogical, Fluid Inclusion, and Multiple Isotope (H-O-S-Pb) Constraints on the Genesis of the Sandaowanzi Epithermal Au-Ag-Te Deposit, NE China.
Economic Geology 113, no. 6 (Sep 2018): 1359-82. http://dx.doi.org/10.5382/econgeo.2018.4605.